# Olefin Polymerization Using Supported Metallocene Catalysts: Process Representation Scheme and Mathematical Model

**DIANA A. ESTENOZ, MARIO G. CHIOVETTA**

INTEC, UNL-CONICET, Güemes 3450,3000 Santa Fe, Argentina

*Received 20 September 1999; accepted 24 August 2000*

**ABSTRACT:** A mathematical model, including the main morphological features of the polymerization process, is developed to study olefin polymerization with supported metallocene catalysts. Because the relatively large amount of methyl alumoxane (MAO) usually needed as a cocatalyst represents a disadvantage, the model introduces a scheme that simulates the results of the efforts being made in a supported catalyst to reduce MAO requirements to commercially acceptable levels. Critical fragmentation steps in the initial support-catalyst particles that render all active sites effectively available to the monomer are specifically considered, on the basis of the support morphological characteristics. With the available reaction data, fragmentation representation alternatives are discussed and a scheme proposed. Then, a mathematical model is developed based on the above representation scheme, to calculate monomer-concentration, temperature, and macroparticle-size evolutions. The main features of the scheme are displayed and discussed. Both for laboratory and high-productivity conditions, the model is used to predict changes in macro- and microparticle size, porosity, and concentration distribution. Predictions are employed to evaluate the impact of the initial support microparticle arrangement and fragmentation processes on the overall catalyst performance. Polymer yield, concentration profiles, and temperature transients predicted by the model are presented, showing the model application after verifying its accordance with the available experimental data. © 2001 John Wiley & Sons, Inc. J Appl Polym Sci 81: 285–311, 2001

**Key words:** mathematical modeling; polymerization; metallocene; supported catalyst; ethylene; fragmentation

## INTRODUCTION

Metallocene-based Ziegler–Natta catalysts with methyl alumoxane (MAO) as the cocatalyst are of scientific and technological interest in the field of $\alpha$-olefin polymerization, since they combine high activity with excellent polymer stereoregularity. Metallocenes are currently the most promising catalytic active sites used for olefin polymerization and the driving force in terms of future applications in grassroot or existing production plants. High activities, relatively narrow molecular weight distribution in the product, low deactivation rates, and, in general, the ability to produce polymers with controlled properties are their main features. Specifically, it has been found that *ansa rac*-Et$[Ind]_2ZrCl_2$/MAO com-

*Correspondence to:* M. G. Chiovetta (mchiove@intec.unl.edu.ar).

Contract grant sponsor: Universidad Nacional del Litoral; contract grant number: CAI+D 12/I122.

Contract grant sponsor: CONICET.

Journal of Applied Polymer Science, Vol. 81, 285–311 (2001)

pounds show very high activity[1] and present high degrees of stereospecificity both in homopolymerization as well as in copolymerization of $\alpha$-olefins.[2,3]

Predictions suggesting a strong increment in the industrial synthesis of polyolefins with metallocene-based catalysts[4] are common in the literature. When homogeneous polymerization is considered, the usual polymer–particle product-separation difficulties are present. Additionally, relatively high operating costs are expected due to the amount of excess MAO needed to obtain the industrially required high activity and stability of the catalyst formulation.[5] Attempts are being made to permanently reduce that ratio to commercially compatible ranges. From a chemical standpoint, in homogeneous polymerization, MAO accomplishes various functions,[6] with the most important being to form a complex with the metallocene, to alkylate it, and to stabilize the cationic metallocene alkyl by avoiding the deactivation effect via bimolecular reactions.

One way of reducing the MAO content in the catalytic system is to immobilize the active complex on a silica support.[7] Support —OH sites anchor the catalytic complex. If the —OH surface density is handled to achieve a given minimum separation between impregnation points, the active sites are isolated enough from one another as to reduce bimolecular deactivation. Additionally, supported catalysts allow an adequate handling of the polymer particles when used in typical fluidized- or suspended-bed polymerization reactors. These types of polymerizers have proved efficient both in terms of transferring the reaction heat out of the bed and of maintaining high levels of catalytic activity throughout the particle residence time, usually in the order of hours, with good product and process control features.

Metallocene immobilization effects on catalytic activity, stereochemistry control, and polymer quality have been experimentally studied.[5,7–9] Nonetheless, the detailed sequence of chemical and physical processes taking place during catalyst preparation is still a matter of discussion.

The purpose of this work was to explore a systematic modeling approach to obtain an adequate representation of the physical–chemical changes in the support-catalyst–polymer solid particle. In particular, the support fragmentation process and the overall polymerization sequence is considered in light of the structural and morphological changes suffered by the silica–metallocene complexes.

## THE CATALYST COMPLEX

Metallocenes can be supported on silica following three different sequences[9]:

1. MAO sorption on silica followed by metallocene impregnation to create a catalytic system of the form $SiO_2$/MAO/Et$(Ind)_2ZrCl_2$ referred to as CCC1 (complete catalytic complex 1). First, MAO reacts to form a stable Si—O—Al bond with the hydroxyl groups remaining on the support porous surface after low-temperature (350/400°C) silica calcination. Then, MAO linked to the support surface removes the $Cl^-$ ion from the Et$(Ind)_2ZrCl_2$ molecule, producing the stabilized methyl *ansa*-zirconocene cationic species.[7]
2. Impregnation of metallocene on silica, without prior addition of MAO, to create a catalytic system of the form $SiO_2$/Et$(Ind)_2ZrCl_2$ or MCC (metallocene catalytic complex). MAO, the cocatalyst, is usually added to the reaction system during polymerization.
3. Metallocene sorption on silica followed by the addition of MAO during catalyst preparation stages to create a system of the form $SiO_2$/Et$(Ind)_2ZrCl_2$/MAO or CCC2 (complete catalytic complex 2).

For cases 2 and 3 above, the manner in which the metallocene is linked to the silica is not well established. However, most authors coincide in accepting the existence of a chemical bond between the support and the metallocene produced through a reactive chemical-absorption process.[5,9]

Values for the experimentally observed activities, compositions, and temperatures for various catalytic complexes are summarized in Table I. Chien and He[7] and Soga and Kaminaka[8] studied the heterogeneous catalytic systems of the CCC1 type (items 1 and 2 in Table I, respectively). The first observation is that activities similar to those in the homogeneous systems (Collins et al.,[5] item 11, Table I) are reached for ethylene/propylene polymerization in CCC1 systems. MAO absorbed onto the support first prevents specific, direct interactions between the metallocene and the support. It has been suggested also that the zirconocene group is relatively mobile above the absorbed MAO units, resembling some of the properties found in homogeneous polymerization.

**Table I Olefin Polymerizations Conducted with $Et(Ind)_2ZrCl_2$ Catalysts**

| Item | Ref. | Commercial Silica Support[a] | Catalytic Complex | Support Calcination Temperature [°C] | % Zr [g Zr/g] | % Al [g Al/g] | $T$ [°C] | [Al]/[Zr] | Activity $[g/h^{-1}\ atm^{-1}\ mol^{-1}\ Zr]$ |
|---|---|---|---|---|---|---|---|---|---|
| 1 | 7 | PQ Corp., g.CS2223, $D_p$ = 40 nm, $S_g$ = 220 $m^2/g$, $V_p$ = 2.2 $cm^3/g$ | CCC1 | 350 | 0.62 | 8.57 | 50 | 670 | $7.7 \times 10^6$ |
| 2 | 8 | Davison, G952, $D_p$ = 20 nm, $S_g$ = 300 $m^2/g$ | CCC1 | 400 | 0.75 | 8.10 | 40 | 500 | $2.6 \times 10^5$ [b] |
| 3 | 5 | Aldrich, G62, 74–250 $\mu$m $S_g$ = 300 $m^2/g$ | MCC (PDS–$AlMe_3$) | 450 | 0.7 | 0 | 29–36 | 2260 | $3.96 \times 10^5$ |
| 4 | 5 | Aldrich, G62, 74–250 $\mu$m $S_g$ = 300 $m^2/g$ | MCC (DS) | 950 | 1.5 | 0 | 28–36 | 743 | $3.60 \times 10^4$ |
| 5 | 7 | PQ Corp., g.CS2223, $D_p$ = 40 nm, $S_g$ = 220 $m^2/g$, $V_p$ = 2.2 $cm^3/g$ | CCC2 | 350 | 0.22 | 4.2 | 50 | 2000 | $2.0 \times 10^4$ |
| 6 | 9 | Davison, G952, $D_p$ = 20 nm, $S_g$ = 300 $m^2/g$ | MCC | 500 | 1.5 | 0 | 50 | 200 | $1.8 \times 10^4$ |
| 7 | 9 | Davison, G952, $D_p$ = 20 nm, $S_g$ = 300 $m^2/g$ | CCC2 | 500 | 0.55 | 6.5 | 50 | 0 | $1.3 \times 10^4$ [c] |
| 8 | 5 | Aldrich, G62, 74–250 $\mu$m, $S_g$ = 300 $m^2/g$ | MCC (PDS) | 450 | 1.46 | 0 | 29–36 | 788 | $1.0 \times 10^4$ |
| 9 | 5 | Aldrich, G62, 74–250 $\mu$m, $S_g$ = 300 $m^2/g$ | MCC (100% OH—S) | 300 | 2.2 | 0 | 25–30 | 250 | 0 |
| 10 | 7 | PQ Corp., g.CS2223, $D_p$ = 40 nm, $S_g$ = 220 $m^2/g$, $V_p$ = 2.2 $cm^3/g$ | CCM | 350 | 0.1 | 0 | 50 | 0 | 0[c] |
| 11 | 5 | None (homogeneous system) | | | | | 60 | 3000 | $2.1 \times 10^6$ |

[a] PQ Corp., Conshohocken, PA; Davison, Baltimore, MD; Aldrich, Milwaukee, WI.
[b] With addition of $AlMe_3$ during the polymerization as cocatalyst.
[c] Without addition of cocatalyst during the polymerization.

An advantage observed for the $SiO_2$/MAO/$Et(Ind)_2ZrCl_2$ complex when compared with the homogeneous system MAO/$Et(Ind)_2ZrCl_2$ is related to the fact that the former reaches high activity levels with much lower MAO quantities. The Al:Zr molar ratio of 1000:10,000 in the homogeneous systems decreases to the 100–200 range for the supported catalysts. The significant difference is attributed to an easier stabilization of the anchored zirconocene, this fact preventing bimolecular deactivation. This effect is analyzed in the section below entitled Amount of MAO Used.

Collins et al.[5] studied the catalyst preparation steps and the polymerization results for MCC systems and propylene. The various supports employed included totally dehydroxylated silica (DS), partially dehydroxylated silica (PDS), partially dehydroxylated silica pretreated with trimethylalumina (PDS–$AlMe_3$), and totally hydroxylated silica (100% OH—S). To reach the various levels of the —OH surface concentration mentioned, calcination temperatures between 300 and 950°C were employed, applying the known fact that the higher the calcination temperature the lower is the —OH concentration. The addition of $AlMe_3$ chemically reduces the —OH amount even further. The various MCC catalytic systems analyzed by Collins et al. for propylene polymerization in the presence of MAO are less active than are soluble catalytic formulations, with metallocenes on PDS–$AlMe_3$ (item 3, Table I) showing the higher MCC activities. In general, it can be observed that MCC activity is higher for lower —OH surface concentrations. For the situation when the support is 100% hydroxylated, no activity was found. This effect can be due to the formation of inactive compounds when metallocenes react with the hydroxyl groups during adsorption.

Kaminsky and Renner[9] studied the preparation and reaction properties of supported complexes of the $SiO_2$/$Et(Ind)_2ZrCl_2$ and $SiO_2$/$Et(Ind)_2ZrCl_2$/MAO type (MCC and CCC2, respectively). The chemical composition of the formulations as well as the polymerization conditions are shown in Table I, items 6 and 7. Activities were considerably lower than were those in the homogeneous systems. With regard to the attained molecular weights (not shown in Table I), they were higher for the MCC and CCC2 systems (30 times higher for polypropylene and five times higher for polyethylene). The same observation can be made concerning the fusion temperature of the polymers obtained. The combination of higher molecular weights and fusion temperatures is of commercial interest given the improvement in the mechanical properties of the produced polymer.

From the analysis of the experimental data for heterogeneous systems in Table I:

1. CCC1 catalytic systems are more active, with production rates comparable to those found in the homogeneous systems but with the advantage of using lesser amounts of MAO since the zirconocene is stabilized through interaction with the supported MAO.
2. CCC2 and MCC complexes are approximately 10–100 times less active than are the homogeneous systems due to irreversible deactivation suffered by the metallocene during adsorption, with a corresponding production of less active sites on the support surface.
3. CCC2 and MCC complexes in Table I produce polymers with higher molecular weights and fusion temperatures, probably due to lower catalyst activity. This observation could be associated with the reduced set analyzed and should not be generalized.

## AMOUNT OF MAO USED

To study the various situations involving the relative amounts of Al and Zr in the systems and to compare these figures with those in homogeneous reactions, three ratios are considered as follows: (i) the molar ratio between Al and Zr in the silica particle after the sorption processes during catalyst preparation steps ($Al_s/Zr_s$); (ii) the molar ratio between Al in the liquid inside the pores prior to monomer addition and Zr absorbed during metallocene impregnation ($Al_p/Zr_s$), and (iii) the molar ratio between Al in the overall fluid phase and Zr absorbed in the solid particle ($Al_f/Zr_s$).

Columns 2 and 3 in Table II show the masses of Al and Zr in the solid catalyst particles after the preparation steps, as reported in the reference for each case. With regard to the $Al_p/Zr_s$ molar ratio, and since in most cases the cocatalyst is fed to the reacting system prior to monomer addition, the Al concentration inside the pore volume of the support when polymerization begins is assumed equal to that in the bulk fluid phase. The third molar ratio, $Al_f/Zr_s$, is calculated using the Al concentration in the bulk fluid phase in the reac-

**Table II Relative Amount of Cocatalyst in Heterogeneous Systems**

| Ref. | % Zr [g Zr/g] | % Al [g Al/g] | $V_p$ [$m^3$/g] | [Al] [mol/L] | $Al_f/Ar_s$ | $Al_p/Zr_s$ | $Al_s/Zr_s$ |
|---|---|---|---|---|---|---|---|
| 7 | 0.62 | 8.57 | $2.2 \times 10^{-6}$ | $3.8 \times 10^{-3}$ | 670 | 0.123 | 47 |
| 8 | 0.75 | 8.10 | $1.7 \times 10^{-6}$ | $5 \times 10^{-3}$ | 500 | 0.110 | 37 |
| 5 | 0.7 | 0 | $2.2 \times 10^{-6}$ [a] | $5.2 \times 10^{-2}$ | 2260 | 1.491 | 0 |
| 5 | 1.5 | 0 | $2.2 \times 10^{-6}$ [a] | $5.2 \times 10^{-2}$ | 2260 | 0.696 | 0 |
| 7 | 0.22 | 4.2 | $2.2 \times 10^{-6}$ | N.A. | N.A. | N.A. | 65 |
| 5 | 1.46 | 0 | $2.2 \times 10^{-6}$ [a] | $5.2 \times 10^{-2}$ | 2260 | 0.715 | 0 |
| 9 | 1.5 | 0 | $1.7 \times 10^{-6}$ | $8.6 \times 10^{-2}$ | 200 | 0.889 | 0 |
| 5 | 2.2 | 0 | $2.2 \times 10^{-6}$ [a] | $5.2 \times 10^{-2}$ | 2260 | 0.474 | 0 |
| 7 | 0.1 | 0 | $2.2 \times 10^{-6}$ | 0 | 0 | 0 | 0 |
| 9 | 0.55 | 6.5 | $1.7 \times 10^{-6}$ | 0 | 0 | 0 | 40 |

[a] Low calcination temperature condition.

tion system containing silica previously impregnated with zirconocene.

All three Al/Zr ratios are listed in Table II, for the conditions in Table I. As can be seen, CCC1 systems show $Al_s/Zr_s$ ratios above or equal to 37. This is aimed at preventing catalyst deactivation by intramolecular reactions affecting the active alkylated zirconocene complex. For this to happen, the $Al_s/Zr_s$ molar ratio must be higher than the average number of repeating units in an MAO oligomer molecule. With the latter usually between 6 and 20 according to Chien and Wang,[6] a 40-fold factor is appropriate.

Although the molar ratio $Al_f/Zr_s$ within the reactor is equal to or higher than 200 for all cases, the pore molar ratio $Al_p/Zr_s$ is very low and, in most cases, even lower than 1. The reason for this low ratio is the locally very high concentration of zirconocene groups on the porous walls (the porous surface is virtually covered by metallocene groups). In the supported sites, practically no additional MAO is needed since the possibility of a bimolecular reaction is low.

All three ratios in the paragraphs above are instrumental in understanding the efficient handling of MAO by the CCC1-supported systems. According to the literature (references in Table I), one of the leading roles for MAO is the prevention of bimolecular deactivation of the zirconocene groups. In homogeneous systems, given the freedom of the metallocene to move within the carrier fluid phase, large amounts of MAO are required to surround zirconocenes and diminish the chance of bimolecular encounters. Supported systems virtually anchor the zirconocenes, thus decreasing the said possibility. However, when —OH anchoring sites are present, another deactivation reason appears through metallocene–hydroxyl interactions. Optimization of the —OH surface concentration is discussed in the section below entitled Effect of the Calcination Temperature on Zr and Al Absorption. Here, some geometry considerations for the CCC1 systems are in order: Assuming from the atomic-size data a footprint for each MAO elementary unit absorbed (—$OCH_3Al$—) in the order of 0.1 $nm^2$ (typical dimensions for the unit range between 3 and 5 Å),[10] the value of 40 found for the $Al_s/Zr_s$ molar ratio indicates that the support surface area is virtually covered by MAO. This means that such a ratio is enough to fully produce the shielding effect that the MAO layer gives the metallocene against —OH deactivation. It also implies that not much additional MAO will be necessary for this effect (low $Al_p/Zr_s$ ratios, as observed). During catalyst preparation steps, and after the porous surface is covered by MAO, no more —OH groups are available for further absorption, and it is very likely that most additional MAO will be washed out during catalyst preparation steps.

Since the metallocene units linked to the MAO-support substrate are not completely free to move after absorption, any additional MAO in the fluid phase will be used mostly for the purpose of enhancing, as a cocatalyst, the activity of the system. In fact, most of this purpose was already achieved by the absorbed MAO. This assertion is suggested by the fact that even with no MAO in the solution the catalyst is still active (item 7, Table I). In CCC1 systems, enough —OH groups are needed to permit the sorption of the relatively large mounts of MAO present.

**Table III Amount of —OH Groups in the Support and Its Effects on Support Typical Dimensions**

| Ref. | System | % Zr [g Zr/g] | % Al [g Al/g] | Zr [mol/nm$^2$] | Al [mol/nm$^2$] | $T_{calc}$ [°C] | OH [#/nm$^2$] | $L_1$ [nm] | $L_2$ [nm] |
|---|---|---|---|---|---|---|---|---|---|
| 7 | CCC1 | 0.62 | 8.57 | 0.1860 | 8.5986 | 350 | 2.95 | 2.3 | 0.58 |
| 8 | CCC1 | 0.75 | 8.10 | 0.1650 | 6.0953 | 400 | 2.35 | 2.4 | 0.65 |
| 9 | CCC2 | 0.55 | 6.5 | 0.1210 | 4.8913 | 500 | 1.80 | 2.9 | 0.74 |
| 7 | CCC2 | 0.22 | 4.2 | 0.0660 | 4.2140 | 350 | 2.95 | 3.9 | 0.58 |
| 5 | MCC | 0.70 | 0 | 0.1540 | 0 | 450 | 2.05[a] | 2.5 | 0.70 |
| 5 | MCC | 1.46 | 0 | 0.3210 | 0 | 450 | 2.05 | 1.7 | 0.70 |
| 5 | MCC | 1.50 | 0 | 0.3300 | 0 | 950 | 0.325 | 1.7 | 1.70 |
| 9 | MCC | 1.50 | 0 | 0.3300 | 0 | 500 | 1.80 | 1.8 | 0.74 |
| 5 | MCC | 2.20 | 0 | 0.4840 | 0 | 300 | 3.55 | 1.4 | 0.53 |

[a] Prior to its treatment with $Al(CH)_3$.

## EFFECT OF THE CALCINATION TEMPERATURE ON ZR AND AL ABSORPTION

The thermal treatment applied to the support particles during the calcination process lowers the —OH superficial content. Table III shows the experimental measurements for the amount of —OH groups per unit surface area for various support systems.[11] The table also shows the number of Zr and Al molecules absorbed per unit surface area for said catalysts and the corresponding lengths $L_1$ and $L_2$ representing the average separation distance between any two adjacent absorbed metallocene molecules and between any two adjacent —OH groups, respectively.

According to the experimental data of Ewwen et al.,[12] the $Et[Ind]_2ZrCl_2$ molecule adopts a spatial arrangement such that it can be considered contained in a volumetric cell with characteristic dimensions in the 1.5–2-nm range. Thus, to avoid the bimolecular reactions involving the activated metallocene molecules and leading to catalyst deactivation, zirconocene units must be separated at least 1.5–2 nm, provided that they are not protected against deactivation by MAO, as in the CCC1 formulations discussed earlier.

The impregnation process includes chemical reactions between the —OH superficial groups and the molecules of either MAO or metallocene, according to the preparation formula. In all cases, from a purely impregnation-oriented standpoint, the largest number of available —OH groups is desirable. However, for MCC and CCC2 systems, a high content of —OH groups may lead to metallocene deactivation because of separation distances falling below those in the range in the paragraph above.

To balance both facts, a trade-off solution is required, with the selection of adequate, intermediate calcination temperatures that render the most useful concentration of —OH groups. As shown in Table III, for calcination temperatures in the 300–500°C range, the —OH content is high enough as to partially deactivate the impregnated metallocene: Distances —OH to —OH between adjacent hydroxyl groups are low enough as to allow some bimolecular deactivation in the MCC and CCC2 systems, where no MAO was affixed first to the support surface. Following this rationale, this type of catalytic system increases its activity with higher calcination temperatures. It can be observed in Table III that for the lower calcination temperature (the higher —OH group concentration) no catalytic activity was detected.

When MAO is absorbed first (CCC1 systems), the —OH groups are chemically linked to the cocatalyst. Since it is necessary to adsorb an amount of MAO large enough to protect metallocenes from deactivation, high concentrations of —OH groups are needed. The subsequent addition of metallocene takes place with much less deactivation, since adsorbed MAO groups shield the metallocene molecules stabilizing them. Consequently, higher activities are observed in CCC1 formulations.

With regard to the molar amount of absorbed Al in CCC1 and CCC2 systems, it is, in general, higher than is the quantity of —OH groups present. This is related to the oligomeric nature of MAO. The repeating unit $(O—AlMe)_n$ has a typical dimension of less than 5 Å. If it is considered that the distance between any two adjacent —OH groups is larger than 5 Å (Wade and Baniester[10]) as shown in the table, the amount of Al absorbed is higher than that of the initial —OH groups,

thus assuring the stabilization of the absorbed metallocene.

## SILICA SUPPORT STRUCTURE AND FRAGMENTATION SEQUENCE

When the $\alpha$-olefins fed into the reactor containing the support-catalyst particles reach the active sites, polymerization proceeds. Monomer transport and reaction as well as polymer accumulation processes take place concurrently with the support-matrix rupture. This breaking phenomenon is relevant to the overall polymerization sequence, since it is the key for maintaining the catalyst productivity throughout the overall particle residence time. Were fragmentation not to occur, extensive regions of the macroparticle including most of the potentially active catalytic sites would not be accessible to the monomer and the polymerization would either stop or become of negligible polymer yield.

Fragmentation is strongly affected by the morphological and structural properties of the support. Its degree of resistance to the forces (related to the mechanical characteristics of the support) exerted by growing polymer molecules and the availability of active sites (related to pore volume, specific surface, and porous size distribution) are critical facts for the rupture process. In fact, particles fragment following various sequences according to their structure. Hence, each support-catalyst structure requires a particular analysis in terms of its physical parameters and structural properties. To account for their impact on fragmentation, the most relevant features of the silica structure are reviewed in what follows. With them, a scheme for the particle geometry able to match the known specifics of the silica/metallocene systems is developed.

Silica-support physical properties such as specific surface, volume, and porous size distribution are controlled and settled during support-preparation steps. Gels used as supports are produced via a process that is schematically shown in Figure 1.[11,13] Silicic acid, $Si(OH)_4$, the starting substance, is unstable in solutions with concentrations above 100 ppm and rapidly polymerizes to form a water–silica matrix through a condensation reaction. First, oligomers of four to five members (—$[Si(OH)_2O]$— units) either in a chain- or closed-ring arrangement are created. This oligomer grows and becomes a silica network by (a) addition of single members, (b) aggregation of other oligomeric chains, and by (c) internal condensation of the hydroxyl groups. In turn, these growing, networklike oligomeric nuclei interconnect themselves to form spherical, nonporous, colloidal elementary particles termed support microparticles or microspheres.

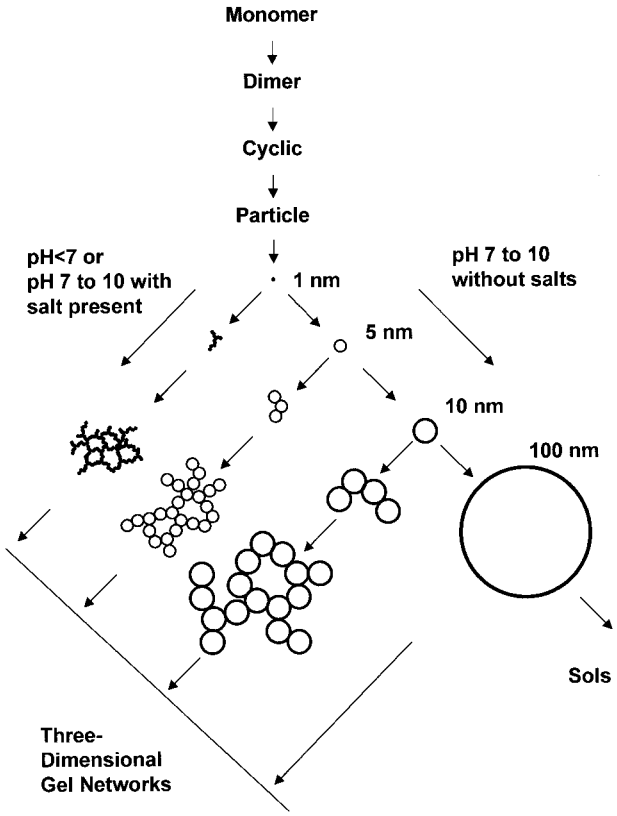


**Figure 1** Formation of silica sols and gels from silicic acid polymerization, after Bergna.[11]

The polymerization rate and the size of these microparticles depend on the solution pH and temperature, being relatively independent of the silicic acid concentration.[11] At room temperature and in an acid medium (pH between 2 and 7), the silica polymerization rate is low, rendering microparticles with diameters in the order of 2–4 nm. For a pH ranging between 7 and 10, polymerization is rapid, and microspheres of 5–10 nm in diameter are formed. For acid concentrations with pH above 10, silica dissolves to form silicates. For higher temperatures, larger microparticles are obtained. Microspheres to 150-nm diameter can be formed with temperatures around 350°C, for various pH values.

In an alkaline environment, the elementary microparticles show negative electric charges, repel each other, and grow as separate units, as

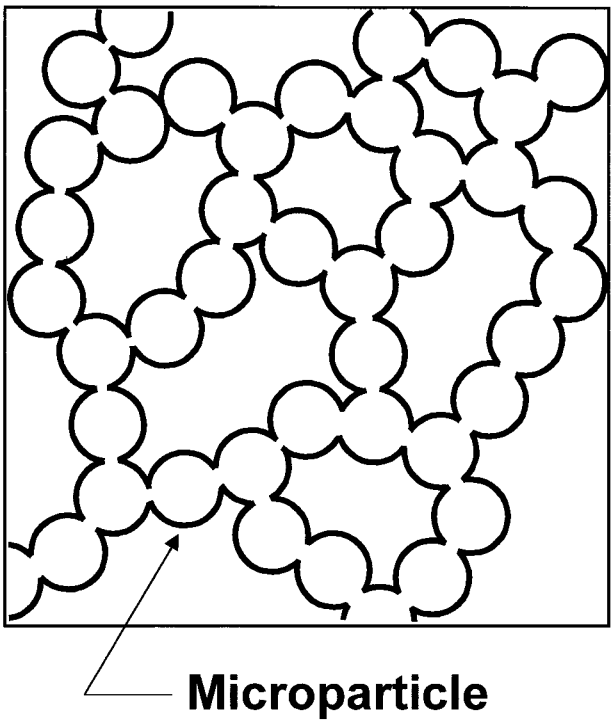


**Figure 2** Silica gel particles formed by the aggregation of microparticles.

shown in the basic medium right branch of Figure 1. Conversely, in acid solutions or if a flocculating salt is added to the medium, particle repulsion decreases and an aggregation process starts to form short chains of (less than 10) microspheres that interact to render a solid lattice and then a gel (Fig. 2).

When the gelling process is completed, the liquid phase is removed by drying to produce a support particle, referred to as a macroparticle, formed by the aggregation of microparticles, linked by both chemical bonds and physical interactions. Temperatures of up to 300–400°C are typical for this stage, with or without a vacuum. While the liquid is being removed from the gel, the remaining silicic acid reacts and additional bonding through —OH condensation reinforces the links between microparticles within the gel macroparticle. Concurrently, the evaporation produces a size reduction in the tridimensional network. In brief, during the drying steps, both the pore volume and the specific area decrease, as the structural properties of the support particle change.

The resulting characteristics of the support particle available for impregnation such as size, concentration, and connectivity of microparticles, porous size, surface area, and pore volume are established by the processing conditions during support preparation such as pH, temperature, and the drying sequence. In Table IV, the most important physical properties of the commercially available support particles used in the studied polymerizations are listed; they will be used to establish the conditions for the fragmentation model.

In general, the support particles in Table IV are characterized by arrangements of small microparticles (1–10-nm-diameter range) showing high porosities and low pore diameters, obtained in a process formed by an acid media precipitation followed by low-temperature calcination as described above in this section. These pieces of data are relevant to establish the structure leading to fragmentation for the silica used as the metallocene support.

With regard to fragmentation, its manner and duration as well as the extent and rate of polymerization strongly depend on monomer access to the active sites. This access is established by the space availability for olefin transport which determines the fragmentation sequence. Two basic arrangements are employed usually:

(a) A scheme of rupture leading to the sequential formation of concentric layers, of the onion-skin type, containing the fragments surrounded and physically linked by polymer molecules. The ruptured support-catalyst pieces segregate from an ever-shrinking support core in a radial, external first

**Table IV Physical Properties of the Support**

| Ref. | Pore Diameter [nm] | Pore Volume [$m^3/g$] | Particle Diameter [$\mu$] | Specific Surface [$m^2/g$] | Porosity |
|---|---|---|---|---|---|
| 7 | 40 | $2.20 \times 10^{-6}$ | 90 | 220 | 0.83 |
| 8 | 20 | $1.70 \times 10^{-6}$ | 70 | 300 | 0.79 |
| 5 | 15 | $2.20 \times 10^{-6}$ | 162 | 300 | 0.83 |
| 9 | 20 | $1.70 \times 10^{-6}$ | 70 | 300 | 0.79 |

mode (REF model[14]). In a support with a small average pore size, the reaction rate is fast and the polymer accumulates rapidly, preferably in the outermost portions of the macroparticle producing the stress required to rupture the links between microparticles. Following the rupture, new monomer paths to inner macroparticle portions are created. The fragmentation process thus created proceeds from the outside to the interior, separating microparticles from the still not fragmented core, establishing an REF rupture pattern. The REF scheme has proved appropriate for polymerizations where magnesium chloride-supported Ti or, in general, Ziegler–Natta catalysts are employed (Ferrero and Chiovetta[15,16]; Chien[17]). For these catalytic systems, the support matrix shows an average porous size below 20 nm, a pore volume below 1.3 $cm^3/g$, and a specific surface below 110 $m^2/g$. Typical calcination temperatures during catalyst preparation steps are lower than 450°C.

(b) A scheme of the internal replication sequence fragmentation (IRSF) type.[18,19] Here, the initial support-catalyst particles break initially into a given number of fragments. These, in turn, fragment again into pieces of smaller size, replicating the initial phenomenon. The process is repeated until a final catalyst fragment (FCF) is reached. If the size of the support pores used as monomer-access channels is large, or if the reaction rate is not extremely rapid, an REF rupture scheme is less likely. The solid matrix, similar to that in a typical Cr active site supported on silica, exhibits a structure fundamentally rich in mesopores. Here, the monomer can access inner sections deep in the macroparticle before polymer accumulation in the pores triggers fragmentation. Thus, large fragments are ruptured, and in each of them, a similar transport–polymerization–accumulation–rupture sequence starts, rendering a replication, the IRSF scheme. With the data in the literature, it can be assessed that the IRSF scheme is a better representation of the real fragmentation sequence when a silica-supported, chromium-based catalyst is considered.[18–20] The most important properties of the Cr-type catalysts supported on silica and used for ethylene polymerizations leading to IRSF fragmentation are a mesoporous structure with average porous sizes between 100 and 150 nm, high pore volume (>1.1 $cm^3/g$), high specific surface (>200 $m^2/g$), very stable structures obtained via calcination temperatures above 900°C, and almost negligible concentration of —OH groups on the pore surface.

For the metallocene catalysts supported on $SiO_2$, there is not enough experimental data available to clearly categorize the fragmentation process as belonging to any of the schemes above or to any other for that matter. Bonini et al.[21] proposed an REF fragmentation scheme, but some of the physical parameters for the solid particle, such as its porosity, were taken from a $Cl_2Mg$ support of a nature different from that in the silica-based one studied in this work

From the data in Table IV and the structural considerations above, it can be seen that, in general, the preparation method for CCC1 silica and typical $Cl_2Mg$ systems is very similar, with small, nonporous microparticles as their main common feature. The low calcination temperature range is instrumental in assuring there are enough —OH groups available on the silica pore surface and allows the pore structure to maintain a pore-size distribution with relatively low average diameters. A high specific surface and a dominant presence of pore diameters equal to or less than 40 nm are the main structural features of the CCC1 systems. Since the physical and chemical events taking place during preparation are similar to those in the Ziegler–Natta catalysts supported on $Cl_2Mg$ that follow REF fragmentation processes, this scheme is likely to command CCC1 fragmentations. However, silica particles in CCC1 systems show initially a higher porosity than that in $Cl_2Mg$ supports in Ziegler–Natta catalytic systems. This significant difference is considered in the model presented below.

In MCC and CCC2 systems, the structural properties will depend on the calcination temperature, in the 300–950°C range, for the data analyzed. For the higher temperatures in this range, the structural and morphological changes during polymerization most likely will follow an IRSF scheme.

## SUPPORT-CATALYST REPRESENTATION SCHEME

After the preparation steps described in the previous section, the support particle in the metallo-

cene catalyst is formed by a set of nonporous microspheres. They are assumed to be arranged in repetitive patterns within the macroparticle, linked following a short-chain arrangement as presented in Figure 2. The porosity of the support particle is related to the manner in which these short chains interconnect themselves to form a tridimensional network, with each microparticle being in contact with a given number of other microparticles. This number was termed coordination number $b$ by Iler[22] and is the key of the representation scheme. The lower the $b$, the looser the network is and, consequently, the higher the resulting macroparticle porosity.

In previous REF models (Laurence and Chiovetta[23]; Ferrero and Chiovetta[15,16]; Hutchinson et al.[24]; Bonini et al.[21]), a support-particle configuration was used where all microspheres were considered arranged in concentric, sequential layers of thickness equal to one microparticle diameter. Hence, the geometric scheme for representing the support particle is established once the density of the microparticle packing in a spherical container (the macroparticle) is selected. Laurence and Chiovetta[23] studied various microsphere-packing arrangements, selecting one in which microparticles are arranged in a square footprint on a spherical layer surface. This arrangement is in good agreement with the experimental data related to porosity and porous sizes in $Cl_2Mg$ supports (void fraction of approximately 0.5). All other arrangements presented in the literature showed porosities below 0.5.

From the data in Table IV, for the silica supports used in metallocene-supported polymerization, porosity is above 0.7. Hence, the arrangements currently available in the literature do not match the experimental data range for metallocene supports.

A geometrical scheme is proposed here to represent silica particles with high porosity, maintaining the short-chain structure for the microparticle arrangement experimentally found. According to the literature, as presented in the previous section, this is the most realistic configuration for the support microparticle network in a macroparticle. Figure 3 shows a schematic representation of the basic cell in the proposed geometrical model. Equal-size, nonporous microspheres of radius $R_C$, interconnected through short-chain links, conform to a cubic pattern. For the case schematically shown in Figure 3, and considering the microspheres termed *A*, *B*, *C,* and *D*, in a short chain forming one edge between any two

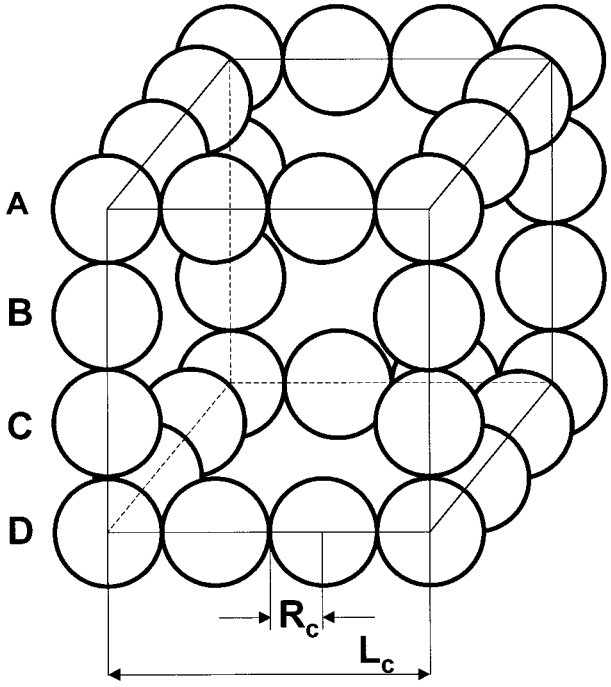


**Figure 3** Schematic representation of the proposed geometrical model.

consecutive vertices in the cube, the coordination numbers $b$ for the spheres are 6, 2, 2, and 6, respectively. The characteristic dimension of this cube is given by $l_c = (2R_C\ n)$, with $n$ being the integer number of microspheres located between two adjacent vertices of the mathematical cube established by the centers of the microspheres in the physical arrangement presented ($n = 3$ in Fig. 3).

The value $(n - 1)$ is the number of microparticles with coordination number $b = 2$ placed between the spheres with $b = 6$ at the vertices of the cube. This cubic arrangement proposed is able to represent various porosities by altering $n$, the short-chain length number, in $n - 1$. The relation between the porosity $\varepsilon$ and $n$, as detailed in the Appendix, is given by

$$\varepsilon = 1 - \frac{3n - 2}{n^3} \times \frac{\pi}{6} \tag{1}$$

Table V shows values obtained with the equation above for various chain-length numbers. As it can be seen from these figures, the proposed scheme is able to model high porosity values within the short-chain pattern representation, in accordance with the experimental ranges available for the porosity of the silica studied.

**Table V Void Fraction as a Function of the No. Microspheres in the Characteristic Dimension of the Cube Arrangement**

| $n$ | $\varepsilon$ |
|---|---|
| 1 | 0.476400 |
| 2 | 0.738200 |
| 3 | 0.864252 |
| 4 | 0.918188 |
| 5 | 0.945546 |
| 6 | 0.961215 |
| 7 | 0.970996 |
| 8 | 0.977502 |
| 9 | 0.982044 |
| 10 | 0.985339 |
| 11 | 0.987805 |

Additional spheres can be added to the basic cubic pattern in the proposed scheme to obtain a more continuous distribution of the void fraction function. The added spheres should have connectivity numbers higher than 2. They will be located, first, in the side faces of the cubic arrangement; only after these spots are covered will the additional spheres fit in the hollow space at the center of the cube. The number of added spheres is termed $a$, varying between 1 and the limiting value $[(n-1)^3 + 3(n-1)^2]$, established by the maximum number of spheres to be arranged in a cube to fill it, to render a porosity equal to that for $n = 1$ in Table V. In general, for $a$ additional spheres accounted for, porosity is given by

$$\varepsilon = 1 - \frac{3n - 2 + a}{n^3} \times \frac{\pi}{6} \qquad (2)$$

Table VI shows the void fraction values for $n = 3$ and various $a$.

The model can be used to obtain the values of parameters required for the calculation of other properties. One such parameter is the microparticle radius $R_C$. From the radius for the macroparticle $R_M$, the porosity $\varepsilon$, and the specific surface $S_{esp}$, the microsphere size can be obtained through (derivation in the Appendix)

$$R_c = \frac{4\pi R_M^3(1-\varepsilon)}{S_{ext}} = \frac{4\pi R_M^3(1-\varepsilon)}{S_{esp} m_M} \qquad (3)$$

Another important length is the maximum and minimum distances between unconnected spheres. These values are given by $[2(n-1)R_C]$ and $[2-1)R_C]$, respectively, and they establish the range for the average porous size of the macroparticle.

The geometrical model above was employed to represent the support particle in the CCC1 catalytic system in Item 1, Table I. The experimental porosity 0.83 according to Table IV is reached using a cubic arrangement with $n = 3$, short chains of connectivity numbers in the sequence 6, 2, 2, 6, and two additional microspheres ($a = 2$) located in the side faces of the cubic arrangement. For the 90-$\mu$m macroparticle, the model predicts a microparticle radius of 6 nm, in accordance with the expected size for the corresponding preparation conditions according to Iler,[22] and a porous size in the range 24–50 nm, in good agreement with the 400 Å reported as average pore size by the PQ Corp. for the catalyst used in ref. 7.

## MATHEMATICAL MODEL

### Proposed Fragmentation Scheme

The fragmentation model presented here is for a catalytic complex of the CCC1 type analyzed above. The analysis is applied to a typical polymerization system such as that in Chien and He.[7] Physical parameters for this system such as porosity $\varepsilon$ and radius $R_M$ are extracted from the data in the first row in Table IV, while the microparticle radius ($R_C = 6$ nm) was calculated in the above section Support-catalyst Representation Scheme. Polymerization activity and conditions are those in the first row in Table I. Other parameters, such as the monomer diffusion coefficient in the fluid medium ($D_L$) and the tortuosity ($\tau$) for

**Table VI Void Fraction as a Function of the No. Additional Spheres Added to a Cubic Arrangement with $n = 3$**

| $a$ | $\varepsilon$ |
|---|---|
| 0 | 0.864252 |
| 1 | 0.844860 |
| 2 | 0.825467 |
| 3 | 0.806070 |
| 4 | 0.786680 |
| 5 | 0.767289 |
| 6 | 0.747900 |
| 7 | 0.728500 |
| 8 | 0.709110 |

**Table VII Monomer Concentration at Various Macroparticles Radii as a Function of Time**

| | $M/M_B$ | | | |
|---|---|---|---|---|
| $t$ (s) | $r/R_M = 0$ | $r/R_M = 0.5$ | $r/R_M = 0.8$ | $r/R_M = 1$ |
| 0.1947 | 0 | 0 | 0.20 | 1.00 |
| 0.7789 | 0.02 | 0.16 | 0.60 | 1.00 |
| 1.9473 | 0.30 | 0.52 | 0.82 | 1.00 |
| 3.8947 | 0.79 | 0.83 | 0.93 | 1.00 |
| 7.7894 | 0.95 | 0.97 | 0.98 | 1.00 |
| 9.7368 | 1.00 | 1.00 | 1.00 | 1.00 |

the macroparticle were taken from the literature.[15,16,18,19]

The model envisions the macroparticle as a pseudohomogeneous medium, where the transport and reaction process is described through the following mass balance equation for the monomer:

$$\frac{\partial M(r_M, t)}{\partial t} = \frac{1}{r^2}\frac{\partial}{\partial r_M}\left\{Dr_M^2\frac{\partial M(r_M, t)}{\partial r_M}\right\} - R(r_M, t) \tag{4}$$

where $M$ is the monomer concentration; $R$, the monomer consumption rate; $r$, the radial position; $t$, the time; and $D$, the effective diffusion coefficient, given by

$$D = \frac{D_L\varepsilon}{\tau} \tag{5}$$

Boundary conditions for eq. (4) are

$$\frac{\partial M}{\partial r_M} = 0, \qquad r_M = 0 \tag{6}$$

$$M = M_B, \qquad r_M = R_M \tag{7}$$

with $M_B$ the equivalent monomer concentration in the bulk fluid phase surrounding the macroparticle.

First, to estimate the monomer degree of accessibility toward the catalytic active site, eq. (4) was solved for the hypothetical case where no reaction takes place ($R = 0$), thus obtaining a purely transport picture. Monomer concentration profiles were calculated under such conditions, with Table VII including the results for some radial positions within the particle at various times.

A generic, order of magnitude diffusion time $t_D$ can be estimated using the results in Table VII, being considered as the minimum period required to achieve full filling of the macroparticle with monomer (equivalent to that needed to achieve a flat monomer concentration profile within the macroparticle). From the calculations, it can be considered to be in the order of 10 s. In a real situation, the values in the time column in Table VII will be substantially higher, since a reaction will be taking place and the monomer concentration will be lower than that in a purely diffusive scheme. Additionally, the polymer mass accumulation was calculated as a function of time for the outermost region of the macroparticle. The experimental, average yield value for the CCC1 catalyst modeled was used ($y = 4.66 \times 10^{-19}$ g/s from Table I). An approximate filling time ($t_f$) is defined as that necessary to reach the situation when enough polymer has accumulated so as to produce the blocking of the monomer flow toward the macroparticle interior. This volume was computed calculating the total number of microparticles in a macroparticle and then assigning to each microparticle an equal fraction of the overall pore volume in the macroparticle. Using again the monomer mass balance for the microparticles in the external region, now including the chemical reaction, the filling time resulted in the order of 2.5 s.

Since this time is considerably less than the minimum diffusion time (10 s), the monomer would be inhibited to reach the inner portions of the macroparticle where the pore-filling process takes place in the exterior layers. When the monomer exterior access paths are blocked, if no fragmentation occurs, the macroparticle polymerization process comes to a halt, since the only active sites still fed by monomer are those placed

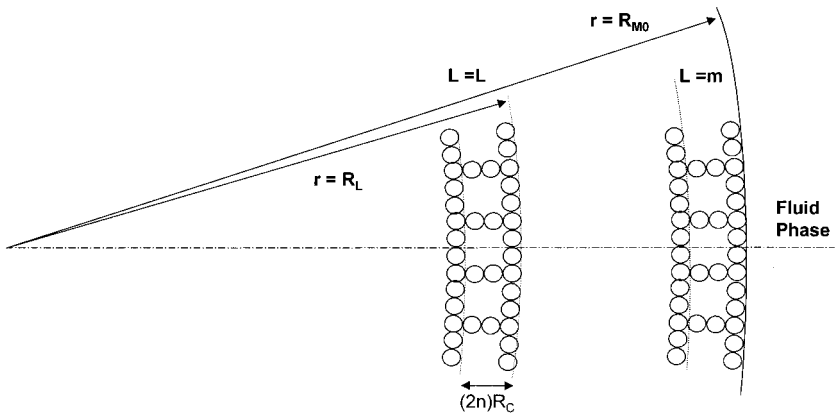


**Figure 4** Microparticle distribution within the initial macroparticle.

on the exterior semisphere of only the microparticles in the very exterior layer.

The experimental information is clear in stating that, even for very long polymerization times (in the order of hours), the catalyst is very active, requiring that the exterior portion of the macroparticle suffers fragmentation. Once the external microparticles are separated from the inner support core, new access paths are formed and the monomer is available to the following concentric fraction of microparticles. Here, the filling process that took place is similar to that previously described for the outermost region, and fragmentation is again required to avoid monomer-pass blocking at this second level. Thus, a second layer is fragmented.

In fact, the catalyst fragmentation process takes place in times shorter than those corresponding to the filling of the access channels. Because of the geometry and space arrangement of the microparticles, there are zones between two microspheres where polymer accumulation can cause tensions high enough to separate the microparticles. These zones are located in the surroundings of the contact points or necks between any two consecutive microparticles. It is required that active sites be placed in this neck area to generate the tensions. For the case of the very active catalytic complexes studied, the active-site superficial density is high. In fact, for the CCC1 formulation being modeled, and according to the figures in Table IV, the support surface is virtually covered by metallocene units.

Due to the support structure and to the transport and chemical reaction sequence, fragmentation occurs because of the accumulation of the polymer in the outermost layers and creates the separation of the microparticles in the said layers. This process must continue toward interior portions of the macroparticle, establishing a pattern that is typical of an REF process.

### Polymerization Model

Rigorous mathematical techniques are applied to follow the transient stages at two calculation levels: (a) global particle (overall support-catalyst–polymer complex) or macroparticle and (b) local phenomena of polymerization at the active sites located in an elementary support unit or microparticle. The initial support-catalyst particle is followed using a multilayer scheme based on the silica representation in this section. A scheme for the arrangement of the particle is presented in Figure 4. Each microparticle layer $L$ in the support-catalyst initial configuration has a thickness equal to $2nR_C$, where $n$ is a function of both the layer porosity and the radial position, according to

$$R_L = (2n)R_C L \tag{8}$$

Considering an initial porosity for the support-catalyst macroparticle of $\varepsilon_0$ and each layer's volume, following the derivation included in the Appendix, the number of microspheres in each layer $L$ is given by

$$N_L = (1 - \varepsilon_0)(2n)^3[L^3 - (L - 1)^3] \tag{9}$$

The initial support-catalyst macroparticle radius $R_{M0}$ is related to the overall number of layers $m$ by

$$R_{M_0} = (2n)R_C m \tag{10}$$

It is necessary to introduce a scheme able to represent the physical changes at any given layer following the effects of polymer accumulation due to the polymerization reaction. The said scheme is described below.

According to the available data for silica, the initial porosity of the support-catalyst macroparticle typically used is high (over 0.75, following Chien and He,[7] Collins et al.,[5] Kaminsky and Renner,[9] and Soga and Kaminaka[8]). However, it is clear that this porosity is larger than that observed in the product particles obtained from the reactors in both commercial and laboratory scales for olefin polymerization (porosity values below 0.5, according to Muñoz Escalona et al.[25] and Webb[26]). Hence, due to polymer accumulation, the macroparticle undergoes morphological changes and does not maintain the structure in the initial configuration shown in this section.

These changes can be explained in terms of the structural characteristics of the support. Initially, and while the monomer has not reacted yet at the active sites, the microspheres are part of a solid network, as indicated in Stage 0 in Figure 5. The rigid nature of the support network during this stage is represented with a full line joining the microparticle centers. Once polymerization begins, and before the fragmentation of the considered layer is completed, the polymer accumulates around support microspheres still bounded by the physical links among them (Stage 1, Fig. 5). When fragmentation occurs, additional degrees of freedom arise. Since the microspheres define a noncompact structure due to the high support porosity, the pressure forces generated by polymer accumulation on their exterior surface are devoted first to breaking the resistance of the solid links represented by the solid lines in Stage 1. These efforts, prior to fragmentation, are mostly concentrated in the macroparticle radial direction and in a direction parallel to the surface of the layer. When the rigid links are broken (in Fig. 5, the lines joining the centers become dotted lines to indicate that the link was broken), a new trend can be observed. Polymer accumulation forces can now generate two effects: (1) a radial growth and (2) a tangential component. The latter creates a sliding effect in each microparticle that now is relatively free to move toward the holes in the initial structure (Stage 3 in Fig. 5). Since more void space is available in these tangential directions, microparticles have the tendency to move following a pattern aimed at filling the voids (tan-

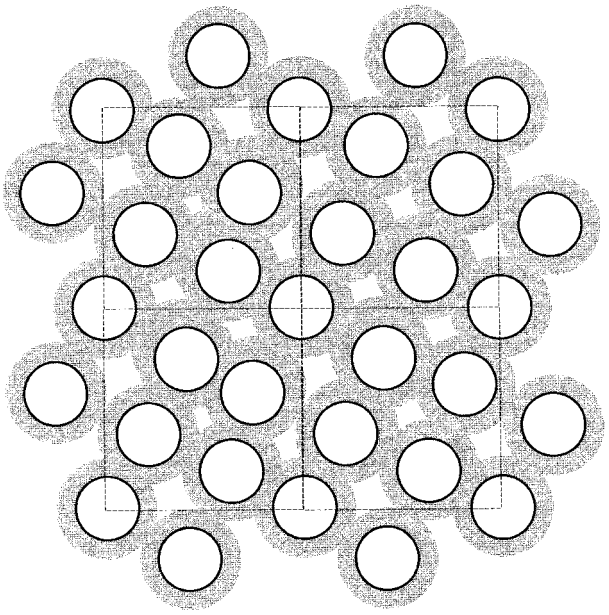

**Figure 6** Overlapping of Stage 4 elements.

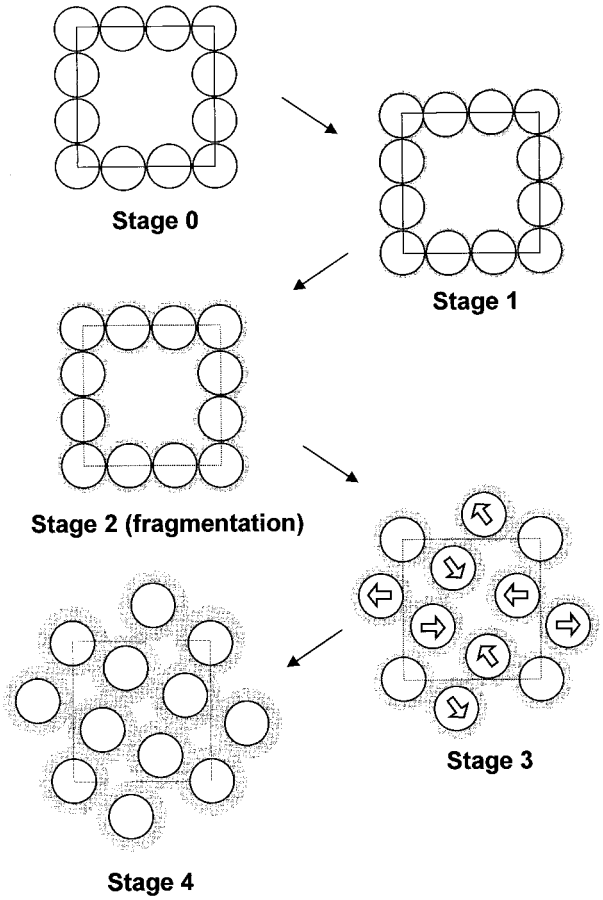


**Figure 5** Void fraction change sequence.

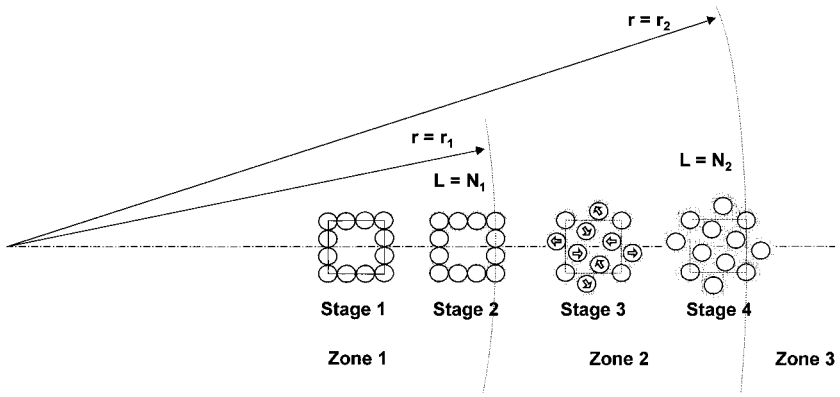


**Figure 7** Various zones within the growing macroparticle.

gential direction) rather than in the radial direction (the generic relative motion direction of each microparticle is represented by an arrow in Stage 3, Fig. 5). Thus, tangential directions dominate the motion of the microparticles during this stage. This appears as a reasonable way of explaining the porosity decay shown during polymerization. The process of accommodation of the microparticles within the network will proceed until the whole region attains a fairly homogeneous compactness in all directions (Stage 4, Fig. 5). From this point on, there is no specific reason for the existence of preferred directions in the microparticle growth/motion. The generalization of the process to a larger region is depicted in Figure 6, where simple overlapping of several elementary units in the Stage 4 scheme in Figure 5 is shown to indicate the repetitive nature of the arrangement attained.

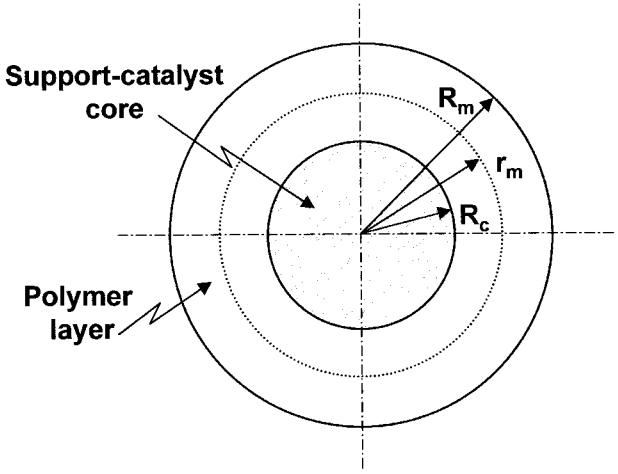


**Figure 8** Schematic of the microparticle representation.

To account for these changes in the mathematical scheme, three regions are identified in the macroparticle (Fig. 7):

*Zone 1:* Catalytic nucleus still not fragmented formed by all layers where polymer accumulation is still not sufficient to produce physical link breakup ($1 \leq L \leq N_1$). In this region, the structure in Stage 1 is maintained and relatively low porosity changes take place by filling of the voids among the microspheres in the rigid initial arrangement. The surface limiting this zone is composed of microspheres with a growth factor $c = c^*$ (growth factor at the fragmentation point).

*Zone 2*: Already fragmented region suffering the particle-accommodation process typical of Stage 3 ($N_1 \leq L \leq N_2$). Here, structural changes occur until the final configuration described in the paragraphs above is reached. The model calculates porosity changes by polymer accumulation, allowing tangential movements in the microspheres until a final porosity $\varepsilon^*$ is reached. The surface limiting this zone is characterized by a porosity $\varepsilon = \varepsilon^*$.

*Zone 3*: The portion of the macroparticle where microspheres have already attained the final configuration. In this region, growth proceeds in every possible direction to maintain the porosity $\varepsilon^*$ (Stage 4 arrangement).

To follow the individual microparticle growth, the scheme in Figure 8 is used for any given microsphere of the initial support-catalyst radius $R_C$, with a polymer layer of thickness ($R_m = R_C$). A growth factor $c_L$ for each microparticle in layer $L$ is defined as a function of a generic macroparticle radius $r_M$:

$$c_L = \frac{R_m(r_M, t)}{R_C} \tag{11}$$

An average growth factor is $\langle c \rangle$ isintroduced in such a way that the overall macroparticle external radius $R_M$ can be calculated:

$$R_M(t) = (2n)mR_C\langle c \rangle \tag{12}$$

With the equations above, the changes in each of the zones in the macroparticle can be followed as a function of the void fraction and the radial position inside the overall growing particle (details in the Appendix):

*Zone 1/Zone 2*

$$\varepsilon(r_M, t) = 1 - (1 - \varepsilon_0)[c(r_M, t)]^3 \tag{13}$$

$$R_L = (2n)R_C L,\ L = 1, \ldots N_2 \tag{14}$$

*Zone 3*

$$\varepsilon(r_M, t)_{\text{zone3}} = \varepsilon^* = 1 - \frac{(V_{\text{solid}})_L}{V_{\text{Layer}}} \tag{15}$$

$$R_L = \left\{ \frac{(1 - \varepsilon_0)}{(1 - \varepsilon^*)} [2nc_L(t)R_C]^3[L^3 - (L - 1)^3] + R_{L-1}^3 \right\}^{1/3}, \qquad L = N_2 + 1, \ldots, m \tag{16}$$

For any given time during polymerization, the overall macroparticle radius and the corresponding growth factor can be calculated using

$$R_M(t) = (2n)R_C \times \left\{ \frac{(1 - \varepsilon_0)}{(1 - \varepsilon^*)} \left[ \sum_{L=N_2+1}^{m} (c_L(t))^3(L^3 - (L^3 - 1)) \right] + (N_2)^3 \right\}^{1/3} \tag{17}$$

$$\langle c \rangle = \frac{R_M(t)}{(2n)mR_C} = \frac{\left( \frac{(1 - \varepsilon_0)}{(1 - \varepsilon^*)} \left\{ \sum_{L=N_2+1}^{m} [c_L(t)]^3[L^3 - (L^3 - 1)] \right\} + (N_2)^3 \right)^{1/3}}{m} \tag{18}$$

The growing support-catalyst–polymer complex is modeled using a pseudohomogeneous scheme over the overall resulting particle referred to as a macroparticle. The pseudohomogeneous scheme represents a solid complex formed by nonporous, support-catalyst solid microspheres covered by a growing polymer stratum (referred to as microparticles) and a porous region through which monomer gains access to the active sites located in the microparticles.

The main model hypotheses are

(a) Spherical symmetry is assumed for each microparticle (Fig. 8) and the overall macroparticle.
(b) The macroparticle is treated as a pseudohomogeneous medium.
(c) Microparticles are evenly distributed within the macroparticle, although arranged in typical regions as shown in Figure 7.
(d) The polymer stratum surrounding each support-catalyst microsphere is considered a pseudohomogeneous medium.
(e) Initial temperature is uniform throughout the support-catalyst macroparticle.
(f) The composition and temperature of the fluid phase outside the macroparticle are uniform and constant.
(g) External mass transfer limitations are neglected (Floyd et al.[27,28]; Estenoz and Chiovetta[18,19]).
(h) Temperature gradients across the polymer stratum surrounding the microspheres are neglected.

Mass and energy balances for the monomer within the macroparticle are given by

$$\frac{\partial M(r_M, t)}{\partial t} = \frac{1}{r_M^2} \frac{\partial}{\partial r_M} \left( \frac{D_L}{\tau} r_M^2 \frac{\partial M(r_M, t)}{\partial r_M} \right) - \frac{R(r_M, t)}{\varepsilon(r_M, t)} \tag{19}$$

$$\frac{\partial T(r_M, t)}{\partial t} = \frac{1}{r_M^2} \frac{\partial}{\partial r_M} \left( \frac{k_M}{\rho_M c_{pM}} r_M^2 \frac{\partial M(r_M, t)}{\partial r_M} \right) - \frac{\Delta H}{\rho_M c_{pM}} R(r_M, t) \tag{20}$$

$$\frac{\partial M}{\partial r_M} = 0, \qquad \frac{\partial T}{\partial r_M} = 0 \qquad r_M = 0, \qquad t = t \tag{21}$$

$$M = M_B; \qquad \frac{\partial T}{\partial r_M} = \frac{h}{k_M} (T - T_B) \qquad r_M = R_M(t), \qquad t = t \tag{22}$$

$$M = 0; \qquad T = T_0 \qquad r_M = r_M, \qquad t = 0 \quad (23)$$

where $M$ is the monomer concentration in the macroparticle porous region; $M_B$, the monomer concentration in the external fluid phase; $T$, the absolute temperature at any given radius within the macroparticle; $T_B$, the temperature in the external fluid phase; $D_L$, the diffusion coefficient in the fluid phase; $\tau$, the tortuosity parameter; $R(r_M,t)$, the polymerization rate expressed as mole of monomer per unit volume and time; $k_M$, $c_{pM}$, and $\rho_M$, the thermal conductivity, the specific heat, and the particle density, respectively; $h$, the external heat-transfer coefficient; and $\Delta H$, the heat of polymerization.

Polymerization is strictly heterogeneous, as the chemical reaction takes place at the active sites located on the external surface of the solid microsphere. As it is part of a pseudohomogeneous scheme, it is modeled as a continuous sink term $R(r_M,t)$. This assumption is reasonable given the existence of a large number of layers in the macroparticle and the very high number of microparticles per layer.

The term $R(r_M,t)$, when written as a function of the layer number and its radial position, is given by

$$R(r_M, t) = \frac{(2n)^3(1-\varepsilon_0)[L^3-(L-1)^3]}{\frac{4\pi}{3}[R_L(t)^3 - R_{L-1}(t)^3]} \times 4\pi R_C^2 k(T) M_C(r_M, t) \quad (24)$$

with $M_C$ the monomer concentration at the active sites and $k$ the kinetic constant per unit area (in m/s), a function of temperature through

$$k(r_M, t) = k(T_0)\exp\left\{\frac{E}{R_g}\left[\frac{1}{T_0} - \frac{1}{T(r_M, t)}\right]\right\} \quad (25)$$

with $E$ being the activation energy and $R_g$ the universal gas constant.

A different calculation level (microparticle level) is required to compute the monomer concentration at the active sites and the growth factor for each microparticle located at any given macroparticle layer. At this level, the mathematical model includes monomer transport across the polymer layer and the chemical reaction at the catalyst active sites located on the microsphere external surface boundary. The monomer is considered as first dissolving into the polymer layer and then moving across its amorphous region. Transport through the crystalline region in the polymer layer is neglected.[26] Additionally, the temperature gradient in the polymer layer is considered negligible.[15,16,18,19,24,27,28]

The following expressions are used to model the transport and reaction processes at the microparticle level:

$$\alpha \frac{\partial M'(r_m, t)}{\partial t} = \frac{1}{r_m^2}\frac{\partial}{\partial r}\left(\frac{\alpha D_{EP}}{\tau_m} r_m^2 \frac{\partial M'(r_m, t)}{\partial r_m}\right) \quad (26)$$

$$\frac{\alpha D_{EP}}{\tau_m}\frac{\partial M'}{\partial r_m} = kM' \qquad r_m = R_C, \qquad t = t \quad (27)$$

$$M' = \eta M(r_M, t) \qquad r_m = R_m, \qquad t = t \quad (28)$$

$$\frac{\partial R_m}{\partial t} = \langle M\rangle \frac{kR_C^2}{\rho_p}\frac{M'(R_C, t)}{R_m^2} \quad (29)$$

where $M'$ is the monomer concentration in the amorphous region of the polymer layer (in mole per unit volume); $\alpha$, the amorphous-phase volume fraction within the polymer layer; $D_{EP}$, the monomer diffusivity in the amorphous polymer; $\tau_m$, the chain immobilization factor; $\eta$, the monomer-in-polymer solubility; $\rho_p$, the polymer density; and $\langle M\rangle$, the monomer molecular weight.

The system of equations for the energy and mass balances at each reaction level as well as the geometry/morphology equations that model the particle growth are solved simultaneously, following the approach in Estenoz and Chiovetta.[18,19] A grid of $m$ points in the radial coordinate is used; at each grid element (radial position), both scheme levels are solved. Concentration and temperature profiles are solved applying a finite-difference scheme,[15,16] in which an analytical–iteration technique[15,16] is employed to account for all changes in the microparticle.

## RESULTS

### Base-case Conditions

The model in the section Mathematical Model was employed to simulate the polymerization of ethylene in a system with metallocene–MAO on a silica catalyst. Simulation conditions are those corresponding to a high-activity laboratory formulation and are summarized in Table VIII. The changes in temperature, monomer concentration,

**Table VIII Parameters for the Base Case**

| Parameter | Value | Units | Reference |
|---|---|---|---|
| $T_0 = T_B$ | 323 | K | Chien and He[7] |
| $P$ | 1.7 | atm | Chien and He[7] |
| $M_B$ | 155 | mol/m$^3$ | Chien and He[7] |
| $R_{M0}$ | $4.50 \times 10^{-5}$ | m | Chien and He[7] |
| $R_C$ | $6.00 \times 10^{-9}$ | m | This work |
| $m$ | 1250 | | This work |
| $k$ | $1.20 \times 10^{-6}$ | m/s | Chien and He[7] |
| $E$ | 13,500 | cal/mol | Estenoz and Chiovetta[18] |
| $\Delta H$ | 20,000 | cal/mol | Estenoz and Chiovetta[18] |
| $\varepsilon_0$ | 0.825 | | Chien and He[7] |
| $\varepsilon^*$ | 0.40 | | Webb[26] |
| $\rho_M$ | $3.96 \times 10^5$ | g/m$^3$ | Reid et al.[29] |
| $\rho_p$ | $9.00 \times 10^5$ | g/m$^3$ | Estenoz and Chiovetta[18] |
| $c_{pM}$ | 0.27 | cal/g K | Reid et al.[29] |
| $k_M$ | 0.47 | cal/m s | Reid et al.[29] |
| $D_L/\tau$ | $5.00 \times 10^{-9}$ | m$^2$/s | Reid et al.,[29] Bonini et al.[21] |
| $D_{EP}/\tau_m$ | $3.33 \times 10^{-11}$ | m$^2$/s | Floyd et al.[28] |
| $h$ | 404 | cal/m$^2$ s K | Floyd et al.[27] |
| $c^*$ | 1.1 | | Ferrero and Chiovetta,[15,16] Bonini et al.[21] |

macroparticle porosity, and polymer yield were calculated as functions of time. These variables were used to follow the transient in the support-catalyst–polymer particle and its changes with regard to geometry and morphology. Overall polymerization time is well in excess of 1 h. The set of parameters in Table VIII corresponds to a situation fairly mild in terms of catalyst activity and energy release, if one compares such conditions with those in an industrial process. The predictions for the latter are discussed later. Simulations predict a polymer yield of 1445 kg of polymer per kg of catalyst after 1.42 h and a corresponding polymer productivity of 1018 kg kg$^{-1}$ h$^{-1}$, consistent with the experimental values of Chien and He.[7]

The profile for the ratio between the monomer concentration at the pores within the macroparticle and the external, fluid-phase monomer concentration is presented as a function of the radius, for various polymerization times. A dimensionless radial coordinate is used defined as the ratio between the actual radial position and the external radius at any given time. It should be kept in mind that the latter varies with time. Results are plotted in Figure 9. The curves are typical of a diffusion and reaction system in terms of shape. The curve for the final time simulated (1 h and 25 min) shows a combination of kinetic and diffusion influences: The concentration distribution is not controlled by either effect. The values at the center of the macroparticle are in the order of one-half the external monomer availability, thus guaranteeing reasonable polymerization rates even for the active sites located at the maximum distances from the fluid phase. A sequence-inversion phenomenon can be observed: The curve for 11 s shows a lower monomer concentration than that for 0.11 s. The variation in the macroparticle structure and the polymerization rate introduces important changes in monomer availability as long as the changes proceed. The inversion can be explained if all variables are pondered simultaneously. The microparticle growth and the support-catalyst fragmentation process must be considered concurrently, as it is described in what follows.

Figure 10 shows a distribution of the growth factor for microparticles located at the dimensionless radius for various times. For the final 5110-s time in the simulations, a fairly even microparticle-size distribution can be observed. The particle diameter varies around 40% when inner- and outermost microparticles are compared, showing good monomer penetration even to the very center of the macroparticle.

Table IX contains the most relevant milestones during the rupture and rearrangement processes

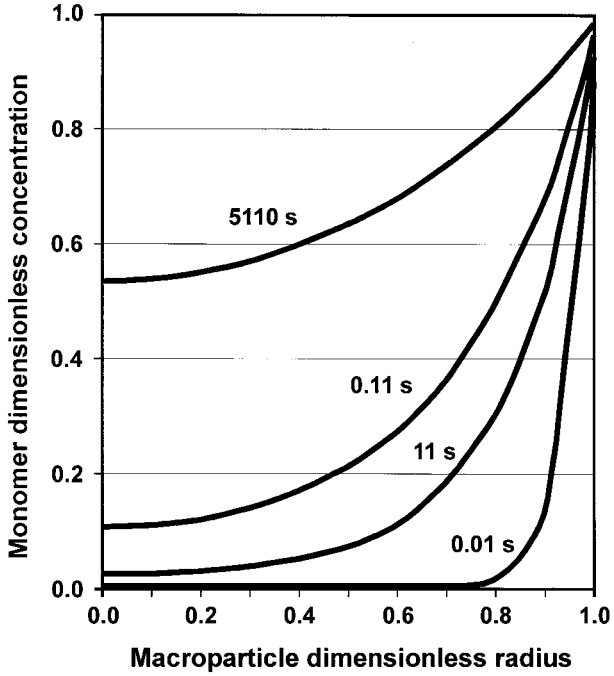


**Figure 9** Macroparticle monomer concentration versus radius at various times for the base case. Conditions as per Table VIII.

discussed in the section Mathematical Models. The position of the limiting surfaces for fragmentation ($c = c^*$) and microparticle arrangement ($\varepsilon = \varepsilon^*$) are reported as functions of time. For the base-case conditions in Table VIII, 0.32 s are needed for microparticles in the outermost layer ($L = 1250$) to accumulate enough polymer mass as to produce the fragmentation of the said layer. At this time, all microparticles in layer 1250 have completed Stage 2 in Figure 5. After 0.32 s, the fragmentation front moves inward, while the microparticles in layer 1250 proceed to Stage 3 in Figure 5. The situation when $\varepsilon = \varepsilon^*$ at layer 1250 arises at 2.29 s, while the completion of the fragmentation process for all of the microparticles in the support-catalyst–polymer macroparticle takes 3.68 s. An overall time of 143 s is needed for the macroparticle to reach the $\varepsilon = \varepsilon^*$ condition throughout its whole volume.

The monomer availability in the macroparticle pores is followed as a function of time in Figure 11, for various layers. In the same figure, the $c = c^*$ and $\varepsilon = \varepsilon^*$ milestones in Table IX are indicated. At any given layer, an initial period can be observed during which the monomer concentration increases, mostly due to diffusion within the macroparticle. A decrease in the rate of accumulation is also seen. This is related to the fact that, although incipient, polymerization occurs; the macroparticle pores start becoming polymer-clogged and monomer transport is affected. Because the physical links between microspheres are not yet broken, the particles cannot react to polymer accumulation by separation, and porosity can only decrease. When fragmentation begins (line for $c = c^*$ at $L = 1250$), links are broken and microparticles can separate. However, the subsequent arrangement process is characterized by a decrease in the layer porosity during Stage 3 in Figure 5, thus affecting the monomer availability even more (arrangement and polymerization processes happening at the same time). When the overall macroparticle is under the $\varepsilon = \varepsilon^*$ condition, the porosity is kept constant while the monomer moves toward the macroparticle center. Diffusion competes with the polymerization reaction to determine the amount of monomer available at any given layer. The hunchback shape in the plots in Figure 11 is the reason for the sequence inversion in Figure 9.

Porosity and temperature evolutions as functions of time are shown in Figure 12. The void fraction, initially at 0.82, decreases to 0.4 after 100 s. Temperature changes are not important, as it should be the case for laboratory conditions.

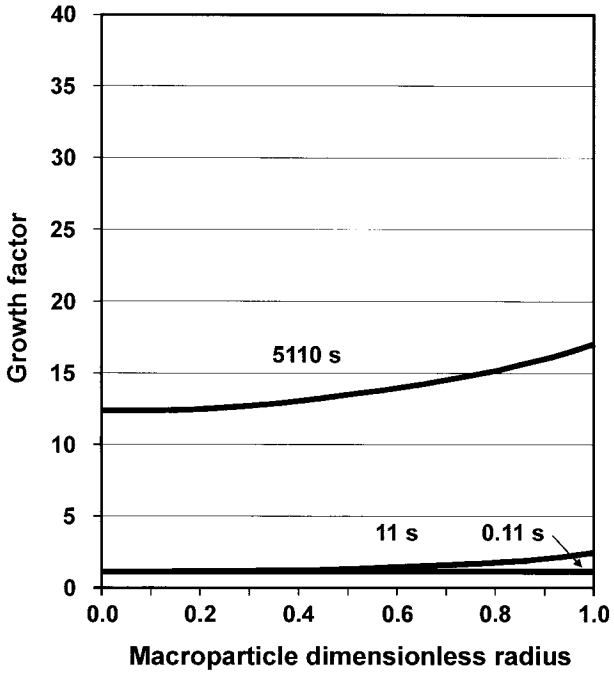


**Figure 10** Microparticle growth factor versus macroparticle radius at various times for the base case. Conditions as per Table VIII.

**Table IX Position of the Fragmentation ($c = c^*$) and Microparticle Arrangement ($\varepsilon = \varepsilon^*$) Fronts at Various Typical Times for the Base Case**

| Time (s) | $c = c^*$ at Layer: | Stage 2 Completed at Layer: | $\varepsilon = \varepsilon^*$ at Layer: | Stage 4 Completed at Layer: |
|---|---|---|---|---|
| 0.316 | 1250 | 1250 | | |
| 2.290 | | | 1250 | 1250 |
| 3.680 | 1 | 1 | | |
| 143.000 | | | 1 | 1 |

The maximum temperature variation is below 2 K. The temperature peak is observed at 0.1 s, with 324.6 K. In fact, thermal conditions are controlled mainly by the heat-transfer coefficient $h$. Following the data in the literature, the Ranz–Marshall and Nelson–Galloway correlations were considered to estimate $h$ for a single sphere in a fluid medium and in concentrated particle-fluid systems, respectively.[27] Both correlations predict similar values for the coefficient when low solid-concentration conditions are employed, such as in the laboratory runs in Table I (volumetric fractions below 0.1). Although laboratory reactors have stirrers, the most conservative condition for the $h$ prediction corresponds to the case when the Ranz–Marshall equation with Nu = 2 is used, assuming negligible relative motion among particles. The value for $h$ in Table VIII was computed in this manner. Even for this conservative assumption, no important thermal effect was predicted by the model.

## High-activity Conditions

Polymerization conditions leading to yields and reactor productivity higher than those in the section above are common in commercial production units. The model was applied to a set of conditions corresponding to a more active catalyst and higher monomer concentrations.

Results for these simulations are presented in Figures 13–16, for the conditions summarized in

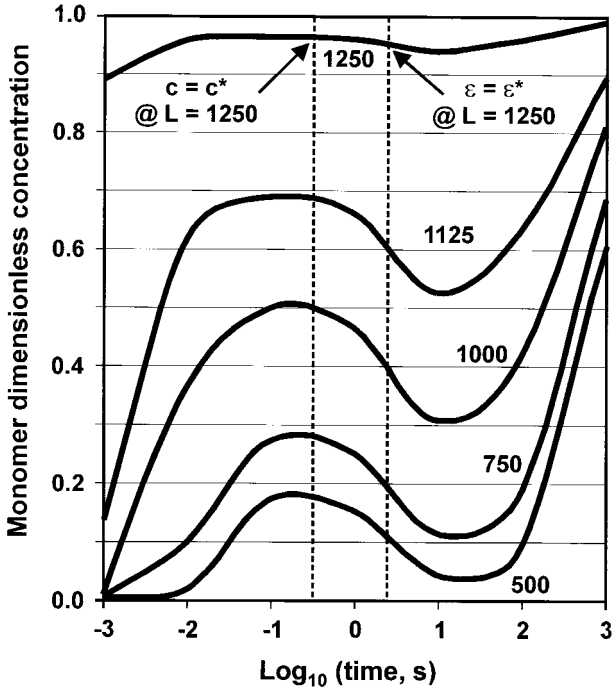


**Figure 11** Macroparticle monomer concentration versus time at various layers for the base case. Conditions as per Tables VIII and IX.

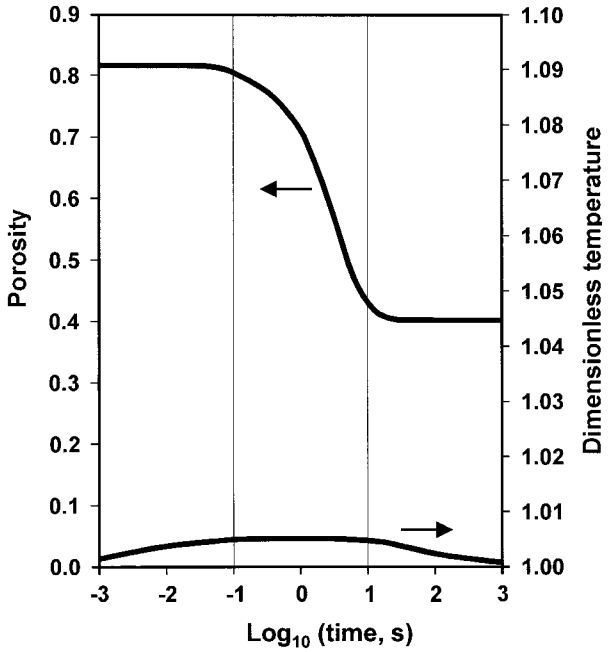


**Figure 12** Macroparticle average porosity and temperature versus time for the base case. Conditions as per Table VIII.

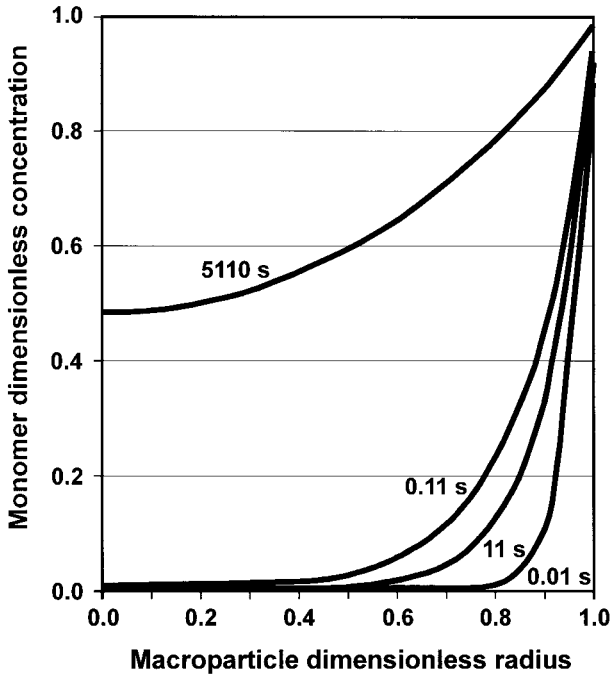


**Figure 13** Macroparticle monomer concentration versus radius at various times. High activity conditions (Table X).

Table X. A kinetic constant equal to $2.4 \times 10^{-6}$ is employed, with a twofold increase when compared with that in Table VIII. Monomer pressure in the gas phase feeding the reaction slurry is increased to 3 atm, in order to reach a concentration in the solvent three times higher. The rest of the parameters are kept equal to those in Table VIII. For these conditions, productivities as high as 5500 kg $kg^{-1}$ $h^{-1}$ are reached.

The concentration profiles in Figure 13 show basically the same trends as those observed in Figure 9, including the sequence-inversion effect. Two observations are worth noting: (a) The curve with the dimensionless monomer distribution for the longest time shown (5110 s) is remarkably similar to that in Figure 9 in terms of the actual concentration at any given radial position; this is an indicator of relatively low diffusion control within the macroparticle pore structure, since the kinetic constant is higher for Figure 13; and (b) for low values of the time parameter, the curves show a stronger effect of the consumption of monomer due to higher reaction rates during the early stages of the macroparticle growth, in particular, while fragmentation is not ended. These results for the concentration are confirmed by the experimental observations with regard to the fact that for long polymerization periods the macroparticle keeps its catalytic activity very high, showing no relevant influence of monomer transport effects within the macroparticle.

Growth factor profiles for various times depicted in Figure 14 are similar to those in Figure 10 in terms of their shapes, although not of their absolute values: As expected for the higher activity conditions, larger microparticles are present. The distribution of sizes is fairly smooth, even for the longest time shown, when the external-to-internal microparticle diameter ratio is in the order of 1.45. With these predictions, it is reasonable to say that microparticles are approximately of the same size across the macroparticle radius. This, again, is coincidental with available experimental data mentioned in the paragraph above. It is also an additional contribution to show the ability of the model to reproducing the known fact that at long polymerization times the reaction capability of each and every active site within the macroparticle remains the same, in spite of longer monomer transport paths to reach the innermost microspheres.

For the concentration curves versus time in Figure 15, the behavior is similar to that for the base case (Fig. 11) with the difference that a stronger diffusion effect is present during all the

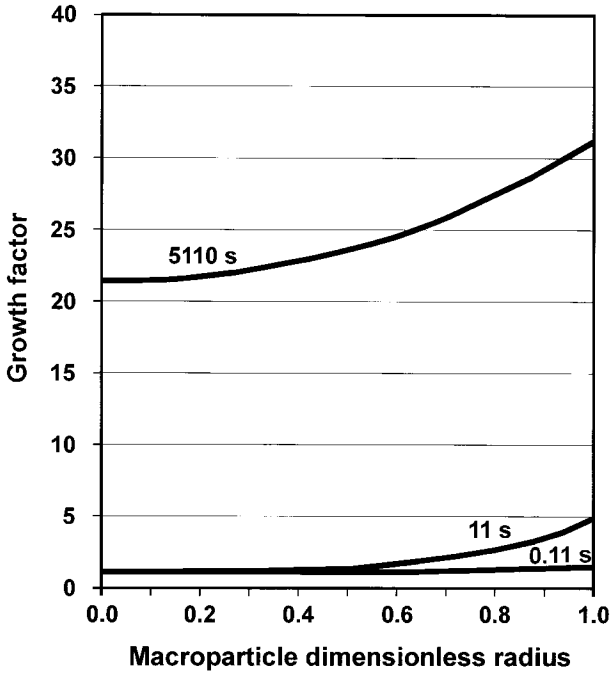


**Figure 14** Microparticle growth factor versus macroparticle radius at various times. High activity conditions (Table X).

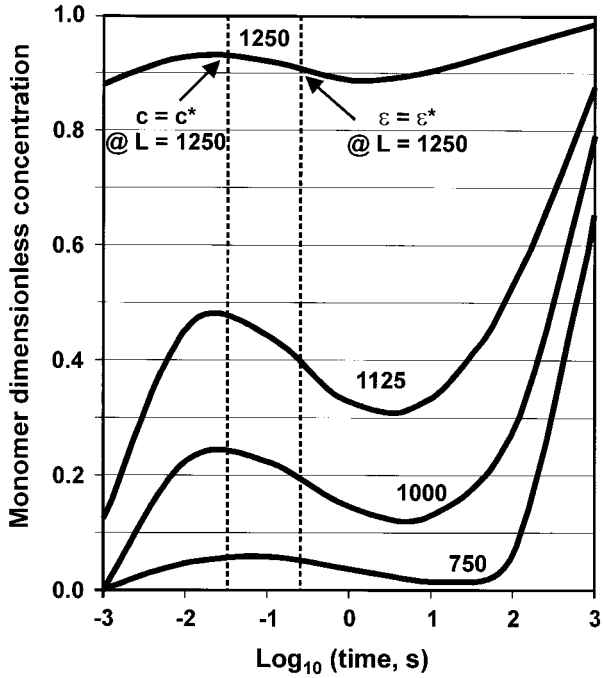


**Figure 15** Macroparticle monomer concentration versus time at various layers. High activity conditions (Tables X and XI).

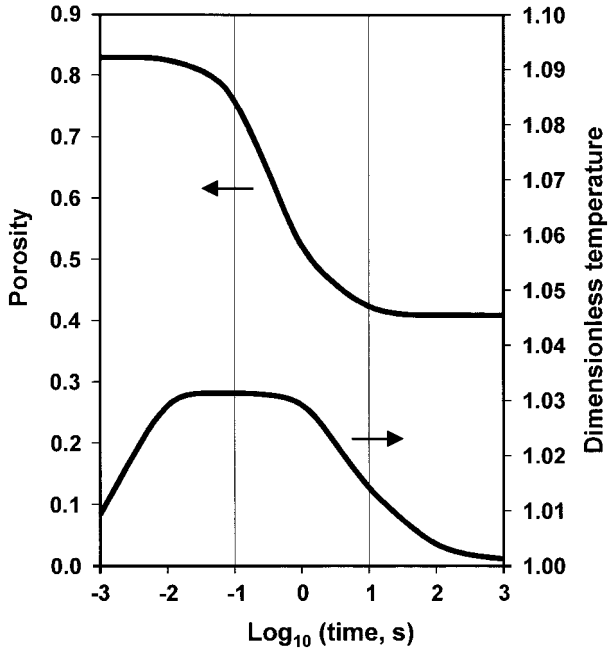


**Figure 16** Macroparticle average porosity and temperature versus time. High activity conditions (Table X).

stages, leading to final rearrangement, because the kinetic constant and the monomer availability are higher (as indicated in Table X). Thus, concentration curves at any given layer show lower values when compared with the base case at equivalent times.

The most important differences with the base case can be observed for the temperature transients within the macroparticle. A maximum value of around 10 K (9.82) is observed for the maximum temperature increase for the conditions in Table X, with a maximum temperature of around 332.82 K. With regard to the value for $h$, the same as in the subsection Base-case Conditions was used for comparison purposes. The effect of temperature during polymerization for more active systems will be discussed elsewhere.

Table XI shows the time required to begin and end the fragmentation and rearrangement stages for the outer- and innermost microparticles. Times vary significantly with respect to those for the base case in Table IX. The influence of the higher activity conditions are stronger during the fragmentation and porosity arrangement transients, now clearly in the hundreds of seconds.

## CONCLUSIONS

A model for the fragmentation process suffered by a polymerizing metallocene on a silica catalytic particle was developed. It is based on the available experimental data and is instrumental in representing the physical and chemical events taking place in the macroparticle during the early stages of the polymerization process.

Various preparation sequences for the preparation of catalytic systems were analyzed in terms of their structural properties and activities. CCC1 systems have shown to be the most active, with polymer yields similar to those in homogeneous formulations, with the advantage or requiring much less MAO due to metallocene stabilization. They are more efficient than are their homogeneous counterparts because they only require enough MAO to cover the support surface and

**Table X Parameters for the High-Activity Simulations**

| Parameter | Value | Units | Reference |
|---|---|---|---|
| $P$ | 5.10 | atm | |
| $M_B$ | 465 | mol/m$^3$ | |
| $k$ | $2.25 \times 10^{-6}$ | m/s | Chien and He[7] |

**Table XI Position of the Fragmentation ($c = c^*$) and Microparticle Arrangement ($\varepsilon = \varepsilon^*$) Fronts at Various Typical Times for the High-Activity Case**

| Time (s) | $c = c^*$ at Layer: | Stage 2 Completed at Layer: | $\varepsilon = \varepsilon^*$ at Layer: | Stage 4 Completed at Layer: |
|---|---|---|---|---|
| 0.034 | 1250 | 1250 | | |
| 0.246 | | | 1250 | 1250 |
| 475.100 | 1 | 1 | | |
| 532.300 | | | 1 | 1 |

their —OH distribution on the support leaves the metallocene units separated enough to avoid deactivation

A geometrical model was presented to closely reproduce the support structure, in good agreement with the experimental data. This geometrical model was used as the framework to predict the nature and velocity of the transport and reaction process involved.

According to the resulting schemes, the proposed fragmentation model predicts the initial polymer accumulation in the outermost portions of the macroparticle. This polymer growth proceeds to an extent large enough as to produce fragmentation in these very regions, even before the inner portions of the macroparticle receive the monomer in a significant amount. After the external layers are ruptured, the process is repeated for the subsequent macroparticle fraction, to allow polymerization to proceed. This process is clearly REF. The model was developed for CCC1 complexes, but can be applied to CCC2 and MCC systems provided that the calcination temperatures lie below 500°C.

Based on this detailed, structural representation for the process, a mathematical model including the diffusion and reaction phenomena was built, to account for mass and energy balances while dealing simultaneously with the structural changes (fragmentation and microparticle arrangement) suffered by each element of the support-catalyst–polymer particle. Treatment of these processes permits the prediction of microparticle size, monomer concentration, porosity, and temperature transients along with polymerization as functions of the radial position in the macroparticle.

The results show a remarkable coincidence with the experimental findings. No diffusion effects, as well as a typical temperature sensitivity, are predicted by the simulations.

The resulting algorithm is set to be employed as a tool for reproducing laboratory conditions and predicting operating conditions in an industrial polymerizer. Such a scheme is able to aid in the startup, operation, control, and optimization of the corresponding industrial vessels.

The authors are deeply grateful to the Universidad Nacional del Litoral (CAI+D 12/I122) and to CONICET for financial support.

## NOMENCLATURE

| | |
|---|---|
| $a$ | number of additional spheres added to the basic cubic pattern |
| [Al] | molar concentration of Al in the reactor ($mol/m^3$) |
| $Al_s$ | Al absorbed in the silica particle (mol/g) |
| $Al_p$ | Al in the pore volume of a catalytic particle (mol/g) |
| $Al_f$ | Al in the fluid phase (mol/g) |
| $b$ | coordination number |
| $c_L$ | dimensionless growth factor for a microparticle in layer $L$ |
| $c^*$ | growth factor at the fragmentation point |
| $\langle c \rangle$ | average growth factor |
| $C_{pM}$ | macroparticle heat capacity ($cal\ g^{-1}\ k^{-1}$) |
| $D$ | effective diffusion coefficient ($m^2/s$) |
| $D_{EP}$ | monomer diffusion coefficient in amorphous polymer ($m^2/s$) |
| $D_L$ | monomer diffusion coefficient in the fluid medium ($m^2/s$) |
| $E$ | activation energy (cal/gmol) |
| $h$ | external heat-transfer coefficient ($cal/m^{-2}\ s^{-1}\ k^{-1}$) |
| $k$ | superficial kinetic constant (m/s) |
| $K_M$ | macroparticle thermal conductivity ($cal\ m^{-1}\ s^{-1}$) |
| $L$ | macroparticle-layer number |
| $L_1$ | separation distance between two adjacent absorbed metallocene molecules (nm) |
| $L_2$ | separation distance between two adjacent —OH groups (nm) |
| $L_c$ | characteristic dimension of a cubic pattern (nm) |

$m$ overall number of layers in the macroparticle
$M$ monomer concentration (mol/m$^3$)
$M'$ monomer concentration in the amorphous region of the polymer layer (gmol/m$^3$)
$\langle M \rangle$ monomer molecular weight (g/gmol)
$M_B$ monomer concentration in the bulk fluid phase (mol/m$^3$)
$M_C$ monomer concentration at the active sites (mol/m$^3$)
$n$ number of microspheres located between two adjacent vertices of a cubic pattern
$N_1$ number of the layer with the outermost, still unfragmented catalytic nucleus in the macroparticle
$N_2$ number of the layer with the outermost catalytic nucleus suffering the accommodation process
$N_L$ number of microspheres in layer $L$
$P$ pressure (atm)
$r_m$ microparticle radial coordinate ($\mu$m)
$r_M$ macroparticle radial coordinate ($\mu$m)
$R$ monomer consumption rate (mol/m$^3$s)
$R_C$ radius of nonporous microspheres or microparticles (m)
$R_g$ universal gas constant (cal/gmol$^{-1}$ K$^{-1}$)
$R_L$ external radius of layer $L$ (m)
$R_m$ radius of microparticle (m)
$R_M$ radius of macroparticle (m)
$R_{M0}$ radius of initial support-catalyst macroparticle (m)
$S_{esp}$ specific surface of macroparticles (m$^2$/kg)
$S_{ext}$ macroparticle exposed solid surface, = $S_{esp}$ $\times$ macroparticle mass (m$^2$)
$t$ time (s)
$T$ temperature (K)
$T_0$ initial temperature of the particle (K)
$T_B$ temperature of the bulk fluid phase (K)
$T_{calc}$ calcination Temperature (°C)
$t_D$ diffusion time (s)
$t_f$ filling time (s)
$V_p$ pore volume (m$^3$/g)
$y$ polymerization yield (g/s)
$Zr_s$ Zr absorbed in the silica particle (mol/g)
[Zr] molar concentration of Zr in the reactor (mol/m$^3$)

### Greek Letters

$\alpha$ amorphous-phase volume fraction of the polymer layer
$\Delta H$ heat of polymerization (cal/gmol)
$\varepsilon$ macroparticle porosity
$\varepsilon_0$ initial porosity of the support-catalyst macroparticle
$\varepsilon^*$ final porosity of the macroparticle
$\rho_M$ macroparticle density
$\rho_P$ polymer density
$\eta$ monomer-in-polymer solubility
$\tau$ tortuosity in the macroparticle
$\tau_m$ chain immobilization factor

### *Abbreviations*

CCC1 complete catalytic complex 1 [$SiO_2$/MAO/$Et(Ind)_2ZrCl_2$]
CCC2 complete catalytic complex 2 [$SiO_2$/$Et(Ind)_2ZrCl_2$/MAO]
MCC metallocene catalytic complex [$SiO_2$/$Et(Ind)_2ZrCl_2$]
IRSF internal replication sequence fragmentation
MAO methylaluminoxane
REF radial, external-first

## APPENDIX

### Derivation of Eqs. (1)–(3)

The porosity in the cube in Figure 3 can be written in terms of the variables in the section Support-catalyst Representation Scheme as follows:

$$\varepsilon = 1 - \frac{V_{solid}}{V_{cube}} \tag{A.1}$$

The cube volume is

$$V_{cube} = L_c^3 = (2R_C n)^3, \tag{A.2}$$

The solid volume in eq. (A.1) can be written using the number of microspheres in the cube in Figure 3, $N_c = 3(n-1) + 1 = 3n - 2$ for any given $n$, and the microsphere volume $4/3\pi(R_C)^3$; by combining these expressions, porosity results:

$$\varepsilon = 1 - \frac{(3n-2)(4/3\pi R_C^3)}{(2R_C n)^3} \tag{A.3}$$

$$\varepsilon = 1 - \frac{\pi}{6}\frac{(3n-2)}{n^3} \tag{1}$$

If $a$ microspheres are added to the cube in addition to those depicted in Figure 3, the number of

spheres become $N_c = 3(n - 1) + 1 + a = 3n - 2 + a$, and, correspondingly, porosity is

$$\varepsilon = 1 - \frac{\pi}{6}\frac{(3n - 2 + a)}{n^3} \tag{2}$$

Finally, a relationship can be established among the specific surface $S_{esp}$ ($m^2$/kg), the macroparticle mass $m_M$, and the microsphere radius $R_C$. First, the overall surface $S_{ext}$ is computed as a function of the number $N_p$ of microspheres in the macroparticle:

$$S_{ext} = N_p 4\pi R_C^2 = S_{esp} m_M \tag{A.4}$$

The porosity can be used to calculate the number of particles:

$$\varepsilon = 1 - \frac{V_{solid}}{V_M} = 1 - \frac{N_p(4/3)\pi R_C^3}{(4/3)\pi R_M^3} \tag{A.5}$$

Solving for $N_p$,

$$N_p = (1 - \varepsilon)\frac{R_M^3}{R_C^3}, \tag{A.6}$$

and replacing into eq. (A.4),

$$S_{ext} = S_{esp} m_M = (1 - \varepsilon)\frac{4\pi R_M^3}{R_C} \tag{A.7}$$

Solving for $R_C$,

$$R_c = \frac{4\pi R_M^3(1 - \varepsilon)}{S_{ext}} = \frac{4\pi R_M^3(1 - \varepsilon)}{S_{esp} m_M} \tag{3}$$

**Derivation of Eq. (9)**

The number of microparticles $N_L$ in any given layer can be calculated using the initial porosity $\varepsilon_0$ and the layer volume. The latter is given by

$$V_L = \tfrac{4}{3}\pi\{(2nR_C L)^3 - [2nR_C(L - 1)]^3\} = \tfrac{4}{3}\pi(2nR_C)^3[L^3 - (L - 1)^3] \tag{A.8}$$

The solid fraction of the layer, a practical manner of using the porosity $\varepsilon_0$, can be expressed as

$$(1 - \varepsilon_0) = \frac{(V_{solid})_L}{V_L} = \frac{N_L(4/3)\pi R_C^3}{(4/3)\pi(2nR_C)^3[L^3 - (L - 1)^3]} \tag{A.9}$$

Solving for $N_L$,

$$N_L = (1 - \varepsilon_0)(2n)^3[L^3 - (L - 1)^3] \tag{9}$$

**Derivation of Eqs. (13)–(18)**

For both zones 1 and 2, the porosity $\varepsilon$ in any given layer at any given time can be expressed as a function of the growth factor $c$ of said layer, using eq. (A.8) for $V_L$:

$$\varepsilon(r_M, t) = 1 - \frac{(V_{solid})_{Layer}}{V_L} = 1 - \frac{(1 - \varepsilon_0)(2n)^3[L^3 - (L - 1)^3](4/3)\pi R_C^3 c^3(r_M, t)}{(4/3)\pi R_C^3(2n)^3[L^3 - (L - 1)^3]} \tag{A.10}$$

Simplification renders

$$\varepsilon(r_M, t) = 1 - (1 - \varepsilon_0)[c(r_M, t)]^3 \tag{13}$$

The radius $R_L$ of any layer $L$ can be expressed in zones 1 and 2 using the initial geometry of the support macroparticle:

$$R_L = (2n)R_C L, \qquad L = 1, \ldots N_2 \tag{14}$$

When entering zone 3, porosity changes to $\varepsilon^*$ and adjustments must be made on the equations for the radius $R_L$ for any single layer in this section and for the macroparticle radius $R_M$. The first step is the recalculation of the porosity in zone 3:

$$\varepsilon(r_M, t)_{zone3} = \varepsilon_L^* = 1 - \frac{(V_{solid})_L}{V_{Layer}} \tag{15}$$

The solid volume in the layer is equal to the number of microspheres in the said layer [$N_L$, eq. (9)] times the current volume of each microsphere including the growth factor $(4/3)\pi[c_L(t)R_C]^3$. The layer volume can be expressed using the $R_L$ variable. Combining these elements, porosity in zone 3 becomes

$$\varepsilon^*(t) = 1 - \frac{(4/3)\pi c_L^3(t)R_C^3(2n)^3[L^3 - (L-1)^3](1-\varepsilon_0)}{(4/3)\pi(R_L^3 - R_{L-1}^3)} \quad \text{(A.11)}$$

After simplification and rearrangement,

$$1 - \varepsilon^*(t) = (1-\varepsilon_0)[2nc_L(t)R_C]^3 \frac{[L^3 - (L-1)^3]}{(R_L^3 - R_{L-1}^3)} \quad \text{(A.12)}$$

Solving for the radius $R_L$,

$$R_L = \left\{ \frac{(1-\varepsilon_0)}{(1-\varepsilon^*)} [2nc_L(t)R_C]^3[L^3 - (L-1)^3] + R_{L-1}^3 \right\}^{1/3}, \qquad L = N_2 + 1, \ldots, m \quad (16)$$

The overall volume of zone 3 is given by

$$V_{\text{zone3}} = \tfrac{4}{3}\pi[(R_M)^3 - (2nR_CN_2)^3] \quad \text{(A.13)}$$

The solid volume in all of zone 3 as a function of the number of microspheres in each layer in the zone, $N_L$, is

$$V_{\text{solid,zone3}} = \sum_{L=N_2+1}^{m} V_{\text{microparticle, Layer L}} N_L = \sum_{L=N_2+1}^{m} [(4/3)\pi(c_LR_C)^3]\{(1-\varepsilon_0)(2n)^3 \times [L^3 - (L^3-1)]\} \quad \text{(A.14)}$$

The expression for the porosity in zone 3 is rewritten using eqs. (A.13) and (A.14):

$$1 - \varepsilon^* = (1-\varepsilon_0) \frac{\sum_{L=N_2+1}^{m} (2nc_LR_C)^3[L^3 - (L^3-1)]}{(R_M)^3 - (2nR_CN_2)^3} \quad \text{(A.15)}$$

Solving for the macroparticle radius $R_M$ renders

$$R_M(t) = (2n)R_C \left( \frac{(1-\varepsilon_0)}{(1-\varepsilon^*)} \times \left\{ \sum_{L=N_2+1}^{m} [c_L(t)]^3[L^3 - (L^3-1)] \right\} + (N_2)^{31/3} \right. \quad (17)$$

The overall, average growth factor defined in eq. (12) can be expressed as a function of $R_M$ above to give

$$\langle c \rangle = \frac{R_M(t)}{(2n)mR_C} = \frac{\left( \frac{(1-\varepsilon_0)}{(1-\varepsilon^*)} \left\{ \sum_{L=N_2+1}^{m} [c_L(t)]^3[L^3 - (L^3-1)] \right\} + (N_2)^3 \right)^{1/3}}{m} \quad (18)$$

## REFERENCES


1. Kaminsky, W.; Miri, M.; Sinn, H.; Woldt, R. Makromol Chem Rapid Commun 1985, 4, 17.
2. Chien, J. J Polym Sci Part A Polym Chem 1991, 29, 1253.
3. Chien, J. J Polym Sci Part A Polym Chem 1991, 29, 1243.
4. Montagna, A. A.; Burkhart, R. M.; Dekmezian, A. H. Chemtech 1997, 26.
5. Collins, S.; Kelly, W. M.; Holden, D. A. Macromolecules 1992, 25, 1780.
6. Chien, J. C. W.; Wang, B. J Appl Polym Sci Part A Polym Chem 1988, 26, 3089.
7. Chien, J. C. W.; He, D. J Appl Polym Sci Part A Polym Chem 1991, 29, 1603.
8. Soga, K.; Kaminaka, M. Makromol Chem 1993, 194, 1745.
9. Kaminsky, W. F.; Renner, F. Makromol Chem Rapid Commun 1993, 14, 239.
10. Wade, K.; Baniester, A. J. In Comprehensive Inorganic Chemistry; Pergamon: New York, 1973; Vol. 12.
11. Bergna, H. E. In ACS Advances in Chemistry Series 234; Urban, M. W.; Grauer, C. D., Eds.; American Chemical Society: Washington, DC, 1994; p 1.
12. Ewwen, J. A.; Haspeslagh, L.; Atwood, J. L.; Zhang, H. J Am Chem Soc 1987, 109, 6544.
13. Weist E. L. Ph.D. Dissertation, University of Massachussetts, 1988.
14. Chiovetta, M. G. Ph.D. Thesis, University of Massachussets, Amherst, 1983.
15. Ferrero, M. A.; Chiovetta, M. G. Polym Eng Sci 1987, 27, 1436.
16. Ferrero, M. A.; Chiovetta, M. G. Polym Eng Sci 1987, 27, 1448.
17. Chien, J. Cat Rev Sci Eng 1984, 26, 613.

18. Estenoz, D. A.; Chiovetta, M. G. Polym Eng Sci 1996, 36, 2208.
19. Estenoz, D. A.; Chiovetta, M. G. Polym Eng Sci 1996, 36, 2229.
20. Mc Daniel, M. P. J Polym Sci Polym Chem Ed 1981, 19, 1967.
21. Bonini, F.; Fraaije, V.; Fink, G. J Appl Polym Sci Part A Polym Chem 1995, 33, 2393.
22. Iler, R. K. The Chemistry of Silica; Wiley: New York, 1979.
23. Laurence, R. L.; Chiovetta, M. G. In Polymer Reaction Engineering on Polymer Properties; Reichter, K. H.; Geiseler, W., Eds.; Hanser: Munich, 1983, p 73.
24. Hutchinson, R. A.; Chen, C. M.; Ray, W. H. J Appl Polym Sci 1992, 44, 1389.
25. Muñoz Escalona, A.; Hernández, J. G.; Gallardo, J. A. J Appl Polym Sci 1984, 29, 1187.
26. Webb, S. W. Ph.D. Dissertation, University of Massachussetts, 1990,
27. Floyd, S.; Choi, K. Y.; Taylor, T. W.; Ray, W. H. J Appl Polym Sci 1986, 31, 2231.
28. Floyd, S.; Choi, K. Y.; Taylor, T. W.; Ray, W. H. J Appl Polym Sci 1986, 32, 2935.
29. Reid, R. C.; Prausnitz, J. M.; Sherwood, T. K. The Properties of Gases and Liquids; McGraw-Hill: New York, 1977.